UNIVERSITÀ DI PARMA

UNIVERSITÀ DEGLI STUDI DI PARMA

DOTTORATO DI RICERCA IN
"TECNOLOGIE DELL'INFORMAZIONE"

CICLO XXXIV

IoT systems for unobtrusive monitoring of physical activity and vital signs

Coordinatore:
Chiar.mo Prof. Marco Locatelli

Tutore:
Chiar.mo Prof. Paolo Ciampolini

Dottorando: Federico Cocconcelli

Anni Accademici 2018/2019 - 2020/2021

"E va bene cervello: tu non piaci a me e io non piaccio a te. Ma facciamola questa cosa così potrò tornare a sbomballarti con la birra!"

Homer Simpson - I Simpson S4:E19 La facciata

Contents

Contents   iii

List of Figures

List of Tables

List of Acronyms

AAL   Active Assisted Living
AC   Aortic valve Closure
ADC   Analog-to-Digital Converter
AFib   Atrial Fibrillation
AO   Aortic valve Opening

BCG   BallistoCardioGraphy
BP   Blood Pressure

CEBS   Combined measurement of ECG, Breathing and
        Seismocardiogram
CMOS   Complementary Metal-Oxide Semiconductor

DAC   Digital-to-Analog Converter
DRL   Driven Right Leg

ECG   ElectroCardioGraphy
EMD   Empirical Mode Decomposition
ESD   ElectroStatic Discharge

FESR   Fondo Europeo di Sviluppo Regionale

FIFO   First In First Out
FIR   Finite Impulse Response

GCG   GyroCardioGraphy

HDF5   Hierarchical Data Format
HDI   Highest Density Interval
HF   Heart Failure
HR   Heart Rate
HRV   Heart Rate Variability

I^2C Inter Integrated Circuit
IM   Isovolumic Moment
IoT   Internet of Things
IP   Internet Protocol

JSON   JavaScript Object Notation

KDE   Kernel Density Estimation

LBNP   Lower Body Negative Pressure
LDO   Low-DropOut
LED   Light Emitting Diode
LPP   Lowest Performance Percentile

MAE   Mean Absolute Error
MC   Mitral valve Closure
MCU   MicroController Unit
MEMS   Micro Electro Mechanical Sensors

MO	Mitral valve Opening
MQTT	Message Queue Telemetry Transport
PCG	PhonoCardioGraphy
PDF	Probability Density Function
PIR	Passive InfraRed
PLEINAIR	Parchi Liberi E Inclusivi in Network per Attività Intergenerazionale Ricreativa e fisica
POR	Programma Operativo Regionale
PPG	PhotoPlethysmoGraphy
PSRR	Power Supply Rejection Ratio
PTT	Pulse Transit Time
PVC	PolyVinyl Chloride
PWM	Pulse-Width Modulation
RIO	Remote Input Output
RMSE	Root Mean Square Error
RTC	Real-Time Clock
SCG	SeismoCardioGraphy
SPI	Serial Peripheral Interface
SRAM	Static Random-Access Memory
TCP	Transmission Control Protocol
TLS	Transport Layer Security
UART	Universal Asynchronous Receiver-Transmitter

Introduction

The last century's advances in medicine, agriculture, technology, and many other fields, significantly impacted human conditions. For example, life expectancy rapidly increased and reached an average value of seventy years [1]. Projections suggest that this increase will continue in the following decades, bringing to older populations. Unfortunately, higher ages mean it is more likely for humans to suffer from cardiovascular diseases [2, 3]. While other factors can contribute to such illnesses, like obesity and diabetes, age alone is a risk factor. With older populations, the rate of heart diseases will increase, thus producing a higher load over sanitary structures and increased costs in public health [4].

Prevention is a valuable resource to reduce the burden on the health system. An example of prevention is to keep people informed about maintaining a healthy lifestyle and engaging them more in healthy activities [5, 6]. Such purpose is shared by the Active Assisted Living (AAL) ideology, which supports the design of services and devices for ageing well. Among the devices and services that fit in the AAL context, there are also the Internet of Things (IoT) technologies, which can be used as a source of healthy stimulus, for example, by identifying sedentary behaviours [7] and suggesting how to have a healthier life, especially to aged persons. However, for such a purpose, IoT devices need to continuously collect accurate data to work correctly. Another form of prevention is to detect the insurgence of an illness before its manifestation [8]. To achieve such a goal, physiological measures can be very useful, but even this approach needs to have the correct data at the right time. IoT devices can be helpful in such a context, allowing for continuous data acquisition. These exam-

ples show how IoT and continuous analysis of activity and physiological data can be a great prevention source because they can constantly provide users and caregivers with helpful information.

Adequate instruments are necessary to obtain valuable and continuous data of subjects' physiological parameters; some are already used and suited for such purposes. For example, the Holter monitor [9] has been used for decades for clinical electrocardiography. Unfortunately, the Holter monitor is not usable over prolonged periods (months or years) because it is uncomfortable and intrusive. Other techniques are more appropriate to that purpose, for example, analysis of SeismoCardioGraphy (SCG) and BallistoCardioGraphy (BCG) signals. Those techniques record mechanical movements induced by heart contraction and blood movements. Compared to the Holter monitor, such techniques can reduce the obtrusiveness or remove it altogether. They do not need any electrode attached to the skin (SCG) or even any device attached to the body (BCG).

Recent technological improvements brought IoT devices like smartwatches into our daily lives. Those devices allow for continuous monitoring possibilities of, for example, physiological information [10], stress condition [11], and sedentary behaviour [12]. The information provided by IoT devices can be complemented by others from different technologies and approaches, enriching the quality of analysis and enlarging the possibilities to detect unhealthy behaviour, the insurgence of anomalies, or possible threats like accidental falls [13]. Surely, a smart floor is an IoT device that can generate interesting information which can complement domestic and wearable technologies. A smart floor is inherently unobtrusive and can provide information like habits, behaviours and activity; moreover, it can be a stimulus to active behaviour if equipped with outputs to interact with the user. Thus it can be a good instrument for prevention.

This work focuses on the study, the research, and the design of IoT technologies suitable for continuous vital sign and activity monitoring in the AAL framework. In particular, here are described two unobtrusive IoT systems designed to improve the quality of life of those who use them. The systems were created for two purposes: the stimulation of active behaviour through activity recognition and the identification of

health problems through continuous monitoring of physiological data. Together, they can provide a broad view of personal well-being and thus uncover the insurgence of possible issues. The first system described is a BCG/SCG system that records and analyses physiological signals to obtain valuable parameters. The second is a smart floor system that stimulates users to keep an active behaviour by providing interactive games.

It is essential to clarify what is not the attempt of this thesis; this work does not attempt to describe medical devices or substitutes for medical devices. The instruments described in this document try to provide new ways to prevent possible problems and consciousness on behaviours that can give a better and healthier life, especially for persons of advanced age.
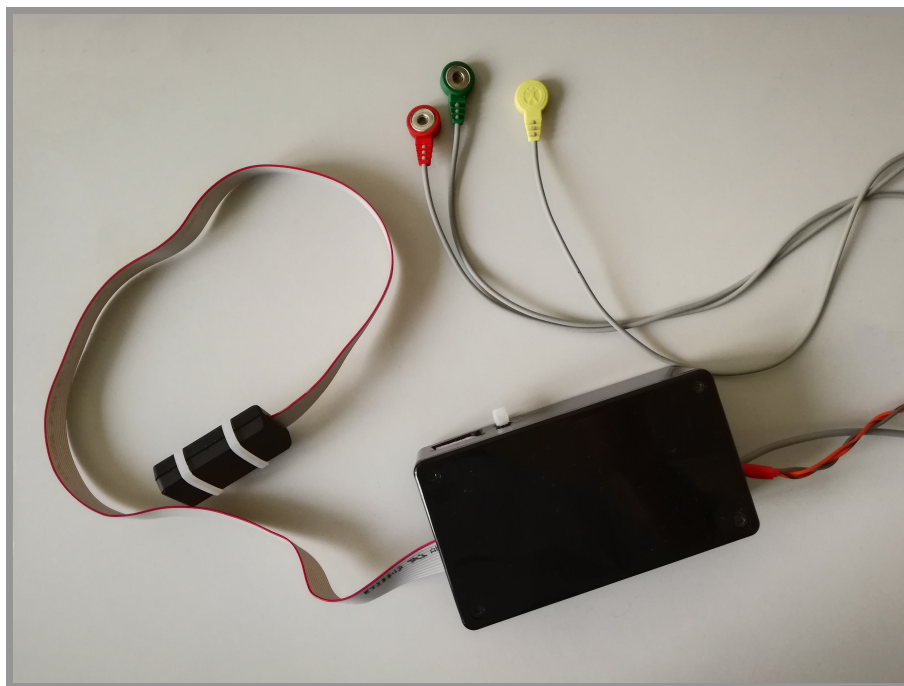
Figure 1: The BCG/SCG acquisition system.

Regarding the BCG/SCG system, the main contribution to the research is the precise identification of heartbeats complexes inside BCG and SCG traces through a unified methodology. The analysis over different datasets suggests that the methods have a high identification ability without providing false beats. Moreover, the research shows another ability: precise time localisation of heartbeats, which allows having reliable beat-to-beat measurements. However, such ability depends on the adopted sampling frequency, which changes the available time resolution and introduces a dependency between precise localisation and energy consumption. Figure 1 shows the device used to acquire BCG and SCG traces.

Figure 2: The Smart floor system.

The second system is a 4 meters large and 2 meters long smart floor; its main purpose is to stimulate active behaviour through interactive games. The novelty of such a device resides in its simple mechanical and modular structure, its high sensitivity to little weights, its orientation towards outdoor use, and its ability to provide different interactive games. The literature lacks smart floors with the same characteristics, to the best of our knowledge. The public tested the device on multiple occa-

sions, always providing great feedback and appreciation. The system was designed in the context of the project PLEINAIR[1] [14] (Parchi Liberi E Inclusivi in Network per Attività Intergenerazionale Ricreativa e fisica), funded by the POR FESR Regione Emilia-Romagna 2014/2020 program. The partners of the project were [15]: DataRiver S.r.l. (leader), University of Parma (Future Technology Lab), University of Bologna (CIRI), University of Ferrara (TekneHub), AIAS Bologna Onlus, Ergotek S.r.l., Sarba S.p.a. and mHT S.r.l. Figure 2 shows the smart floor system and other elements of the project.

The following chapters introduce continuous vital sign and activity monitoring and explain the attempts to build devices suitable for that purpose. Chapter 1 gives a panoramic of the different methodologies for continuous vital sign and activity monitoring. Chapter 2 describes the methods and devices used to identify physiological parameters. The focus of Chapter 3 is on the description of instruments and methodologies used to build a smart floor for activity monitoring and well-being stimulus. Inside Chapter 4 are discussed the analysis results of the proposed devices and methodologies. Finally, Chapter 5 compares the work with others in the literature, describes future developments, and concludes.

---

[1] https://www.youtube.com/watch?v=Yr_0RcdNOjE

Chapter 1

Continuous activity and vital signs monitoring

This chapter introduces the different methodologies that can be used to monitor physiological parameters and activity continuously. In particular, significant focus is placed on BCG and SCG signals and smart floors, the two main themes of this work.

1.1 Continuous vital sign monitoring

Nowadays, smart devices are starting to be part of domestic environments; their presence promotes the development of innovative services. Following the AAL paradigm, such services can increase safety and support the life of people with disabilities or older adults. A wide range of technologies and services fit inside the AAL context, from telemedicine [16] to unobtrusive and continuous monitoring [17]. Some of those can compensate for the troubles introduced by diseases, like home control through Brain-Computer Interfaces for motion impaired users [18], or vocal assistance for a person with visual impairments[19].

Wearable devices fit inside this scenario and, through various solutions, can provide a continuous collection and analysis of vital signs like Heart Rate (HR) and Blood

Pressure (BP) [20] or physical activity. A perfect example of IoT technology that offers such features is the smartwatch [21, 22]; nevertheless, continuous HR monitoring through PhotoPlethysmoGraphy (PPG) can have limitations in wearing comfort and measuring accuracy [23, 24], thus in vital signs estimation.

However, due to the importance of heart information in clinical applications, the gold standard used for HR measures is ElectroCardioGraphy (ECG). Unfortunately, such a technique is unsuitable for prolonged periods outside clinical contexts. Thus, providing a different way to obtain physiological information can be worthwhile, for example, through SeismoCardioGraphy (SCG), which studies the mechanical vibrations created by the heart expansions and contractions. An accelerometer placed upon a person's sternum can thus provide HR and Heart Rate Variability (HRV) measures. Moreover, SCG signals contain cardiac output and heart valves dynamics information. Instead, BallistoCardioGraphy (BCG) can provide heart information through non-contact measures, studying the vibrations that are propagated by an object mechanically coupled with the person, like a bed, a chair or a weighing scale.

The following paragraphs describe the signals mentioned above, contextualising their use in the various works discovered in the literature.

1.1.1   Electrocardiogram - ECG
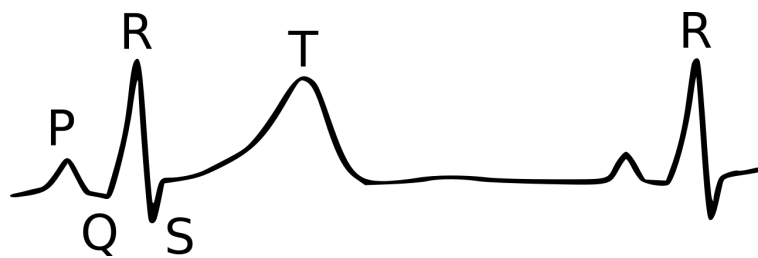
Figure 1.1: The typical ECG pattern.

An electrocardiogram records the heart's electrical activity, acquired through electrodes applied to the subject's skin. Such electrical activity is due to the polarisation and depolarisation of the cardiac muscle. The cardiac events are strictly correlated

to the ECG waveform and its points. Figure 1.1 shows a typical ECG waveform with its main points annotated. Through ECG, it is possible to obtain physiological parameters like HR and HRV. However, this technique is prone to artefacts that can distort the measures, thus needing ad-hoc methodologies to reduce the impact of such a problem [25, 26]. The authors of [27] adopt appropriate filters for different types of noise inside ECG waveforms and provide heart condition classification. Instead, Inoue et al. [28] examined noise generation in printed textile probers suggesting a particular way to make the electrodes.

Through deep learning techniques is possible to identify mechanical dysfunction and abnormal heart rhythms, to guide and support caregivers' decisions [29]. Even authors of [30] propose deep learning techniques applied over ECG signals, but for biometric human identification. Used conjunctly with other typologies of signals, like oscillometric measures, ECG can provide blood pressure information [31, 32]. These physiological parameters can be obtained if heartbeats are identified precisely and correctly inside the ECG traces. Jiapu Pan and Willis J. Tompkins approached the problem many years ago, proposing the Pan-Thompkins algorithm [33]. In more recent years, other authors proposed a solution for heartbeat identification [34, 35].

Even though ECG offers a broad spectrum of possibilities, its use is not suited for continuous monitoring outside clinical contexts. Indeed, it is uncomfortable and intrusive due to the necessity of electrodes attached to the body. However, in the latest years, wearable technologies, like the Apple watch[1] from Apple, or ear-worn devices [36], have significantly reduced the burden of this type of measure.

---

[1]https://www.apple.com/it/watch/

1.1.2 Seismocardiogram - SCG
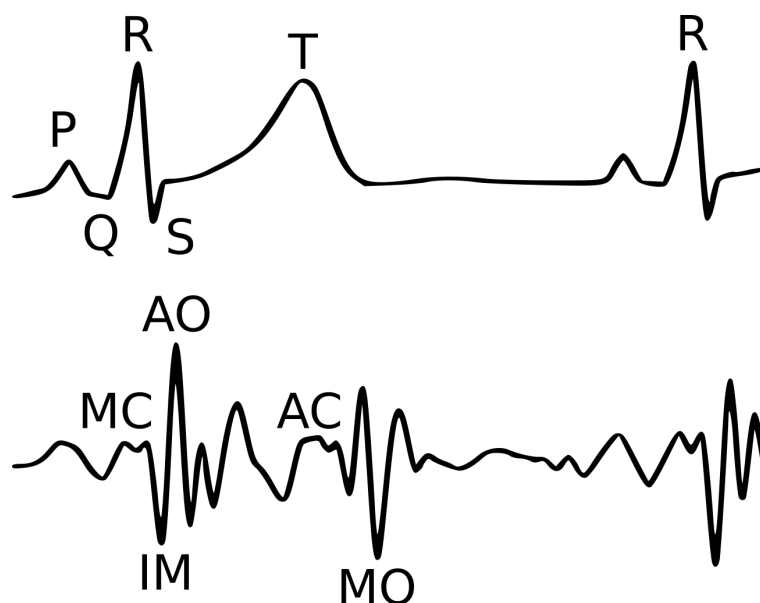
Figure 1.2: Typical SCG pattern and cardiac moments correlated with an ECG waveform.

Seismocardiograms are oscillatory signals originating from the vibration induced by the contraction and expansion of the cardiac muscle and transmitted to the chest. The seminal work of Salerno and Zanetti [37, 38] firstly investigated this field, which gained popularity thanks to the advent of MEMS (Micro Electro Mechanical Sensors) technology [39]. Usually, the device sensing the vibrations is placed over the subject's sternum, and the magnitude of the signals is of few milli-gs (where g is the gravitational acceleration) [40, 41]; however, direct contact is not mandatory, as the authors of reference [42] demonstrate presenting a device capable of day-long acquisitions.

Recently, different works in the literature have focused on SCG to complement and augment the information provided by ECG [43]. As for ECG, even SCG signals need methodologies to segment the waveforms and identify heartbeat complexes; some

work addresses such problems using ECG supervision [44]; in previous work, we accomplished it without supervision [45]. Even other works [46] achieved heartbeats annotation without using the ECG signals.

Through ultrasound imaging validation [47] and echocardiogram [48], cardiac phases were linked to some points inside the SCG waveforms confirming its ability to complement ECG information. Figure 1.2 shows a typical SCG waveform correlated with an ECG; heart moments are marked over the SCG trace, in particular: Aortic valve Opening (AO), Aortic valve Closure (AC), Mitral valve Opening (MO), Mitral valve Closure (MC), and Isovolumic Moment (IM). For a deep analysis of the heart condition, it is important to mark such points precisely; in [49], the authors developed an automated method to identify IM and AC moments.

SCG proved to be a valid signal for Atrial Fibrillation (AFib) detection. Through the training of a classifier on HRV and SCG spectral entropy features, the authors of [50] were able to detect AFib. Instead, the use of Deep-learning networks allowed to obtain signals' information [51] and assess Heart Failure (HF) patients' clinical status [52].

With the same setup as SCG, gyroscope sensors can be used to study heart dynamics [53]; such technique was named GyroCardioGraphy (GCG), accordingly. Authors of reference [54], combined the information of SCG and GCG to identify cardiac events inside the waveforms. The authors of [55] obtained heartbeat detection through the same couple of signals. Again, the same signals were used in [56], authors show the possibility of AFib detection using smartphones. Instead, the work of Yang et al. [57] explored the correlation between fiducial points inside SCG signals and GCG waveforms.

SCG and GCG signals are prone to artefacts [58], especially from body movements, due to the mechanical nature of the signals. Some works focused on artefacts reduction; in [59], are compared different denoising techniques. The authors find that wavelet thresholding achieves the best results on signal enhancement and computational efficiency. Instead, through Empirical Mode Decomposition (EMD), the authors of [60] reduced the noise created by walking.

1.1.3 Ballistocardiogram - BCG
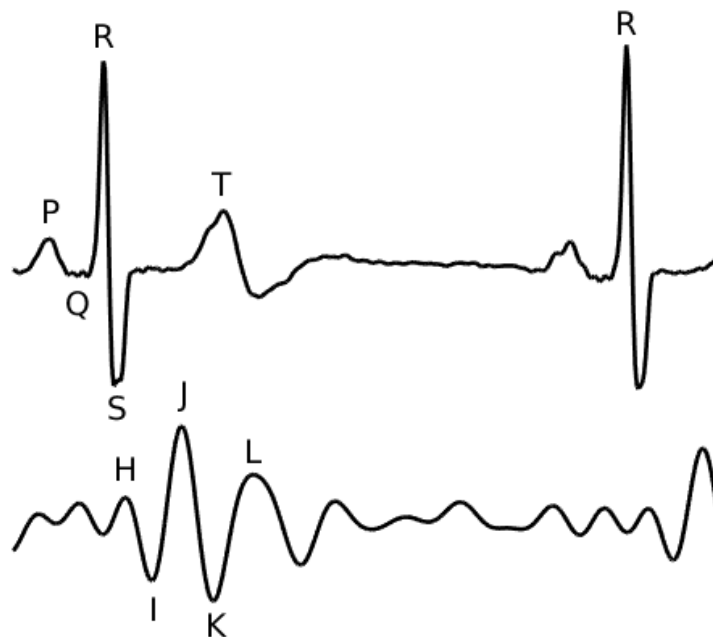
Figure 1.3: Typical BCG pattern and its principal points correlated with an ECG waveform.

The study of BCG goes back to Starr's seminal work [61]. BCG originates from the recoil forces due to the movement of the blood inside the cardio-circulatory system. Figure 1.3 shows a typical BCG pattern correlated with an ECG signal. As for SCG, even BCG gained popularity thanks to technological improvements in MEMS devices and other typologies of sensors [62]. However, compared to SCG, BCG's setups are different in placement, sensors, and technology. For example, the authors of reference [63] obtain Pulse Transit Time (PTT) quantities utilizing a wrist-worn BCG sensor. Instead, a BCG is obtained from different positions on the body (upper arm, knee and wrist) and its potential to identify heart moments like AO and AC is investigated [64]. Another way to measure BCG is through non-wearable devices, which sense vibrations transmitted to objects mechanically coupled to the subject's

body. Examples are a bed [65], a weighing scale [66], or a chair [67]. Various sensors can detect the vibrations propagated through the objects, like accelerometers [68], force plates [69], load cells [70], piezoelectric sensors [71] and optical fibers [72, 73]. Recording through objects is not the only possibility to obtain BCG signals; even artificial vision techniques can be adopted for non-contact measures [74, 75].

Reference [76] presents an interpretative model for BCG. Such a model can simulate different heart conditions' effects over the BCG waveforms, like increased stiffness and reduced left ventricle contractility. Another mathematical model [77] suggests that the principal mechanism that generates BCG is blood pressure gradients in the aorta.

BCG measures are influenced by posture [78]; authors of reference [79] compare different setups and propose a computational methodology to reduce such an effect.

As for SCG, identifying the BCG complexes inside the waveforms is essential for physiological information extraction. In the literature are proposed different methodologies to solve the problem, like the ones of Brüser et al. [80], Lee et al. [81] and Lydon et al. [82]; in reference [83], such approaches are compared on two datasets. Results show that the methods adopted in [80] provide the best results in terms of detection rate and annotation accuracy. Another approach is described in reference [84], where signals recorded from a chair headrest are processed through multi-resolution wavelet analysis. The authors state that their methodology has a computational advantage and improves noise filtering compared to EMD techniques.

Through BCG information, different works presented methodologies to discover abnormal conditions. Reference [85] tries to discriminate between AFib and sinus rhythm utilising machine learning algorithms. By combining BCG and ECG signals, it is possible to detect changes in BP; the authors of [86] developed a classifier to distinguish changes in systolic BP to detect orthostatic hypotension and supine hypertension. Due to the possibility of being recorded from beds, BCG is suited for sleep analysis like sleep breathing disorders [87], classification of sleep-wake state [88], and sleep efficiency estimation [86].

Table 1.1 shows a summary of the main possibilities offered by SCG and BCG.

Table 1.1: Resume of the main possibilities offered by SCG and BCG

Methodology	Source of signals	Coupling	Possibilities
SCG			
	Vibrations induced by heart contraction	Direct contact Textile vest	AC, IM moments detection AFib detection HRV and HR measure
BCG			
	Vibrations induced by blood's recoil forces	Direct contact Bed Weighing scale Chair	AO, AC moments detection AFib detection Sleep analysis PTT measure BP measure HRV and HR measure

1.1.4   Some words on other techniques

In the context of continuous vital sign monitoring, other techniques find a place. Some, like photoplethysmography and PhonoCardioGraphy (PCG), have been used clinically for many years. Modern research try to reduce the necessity of contact measures by adopting new technologies, like radar systems [89], to identify heart sounds. Through an airborne pulse-Doppler ultrasound system, authors of reference [90] achieved heart rate detection on subjects with clothes. Instead, Villarroel et al. used cameras to monitor infants inside a neonatal intensive care unit and obtain heart rate, respiratory rate, and changes in oxygen saturation continuously [91]. Authors of [92] introduce a new principle that allows having accurate remote measures of blood oxygenation even in the presence of significant subject motion. Measures of HRV can be obtained from PPG recordings, as findings of reference [93] suggest. Coupled with ECG, PPG signals can continuously and unobtrusively provide BP; authors of [94] present their cuffless nonintrusive approach. Instead, Carek et al. [95] show that even coupling BCG signals with PPG ones allow for esteeming blood pressure; their setup involves a BCG acquired from a weighing scale and a PPG acquired from the

foot. Photoplethysmography also provides information on respiratory activity, in [96] authors describe an algorithm capable of extracting such information.

1.2 Continuous activity monitoring

In the field of continuous activity monitoring, some different technologies and methodologies can provide a large variety of instruments and services beneficial for the various necessities of daily living, especially for elderly care [97]. For example, the works of Errico et al.[98] and Mancini et al. [99] focused on the reduction of the problematics that motion impairments bring in everyday life; instead, Andò et al. developed a smartphone-based solution to classify daily activities and identify problems, like an accidental fall.

Wearable devices can bring information on the activity and localisation of a person [100, 101] and suggest how to keep a better lifestyle. In [102] authors show the benefits that localisation and activity recognition can have inside AAL technologies, particularly for frail people with Alzheimer's disease.

Unfortunately, wearable systems always face the obstacle of obtrusiveness which is critical for accepting a technology. However, other methodologies can provide similar information. In reference [103], the authors use a variety of non-invasive sensors placed in the domestic environment to obtain information about the health conditions of the subject. Among non-invasive devices for daily life activity monitoring, take place smart floors.

1.2.1 The potential of smart floors

The use of smart floors involves a multiplicity of fields, for example, entertainment, power generation, localisation, and activity monitoring. Because of its potential, already two decades ago Orr et al. used a smart floor to study people identification and tracking [104]. Footstep recognition through a sensible floor was studied some years before, in 1997 [105]. Recently, smart floors were studied in another research to distinguish footsteps among other events [106]. Instead, the authors of [107] designed a modular interactive floor able to provide entertainment through multimedia

and games. Smart floors can be used to address the problem of fall detection, which is what the works presented in [108] and [109] address together with localisation. Framed inside the AAL perspective, localisation could help to provide innovative and useful services. However, such a feature must address privacy issues and concerns, especially inside domestic environments. In this regard, compared with a tracking system that uses video cameras, a smart floor is an optimal solution. To provide localisation features to their smart floor, Feng et al. used fiber optics [110]; instead, the authors of [111] used Passive InfraRed (PIR) sensors and force-sensing resistors.

Daily activities can tell a lot about personal wellbeing and health, thus, technologies able to identify and track them through time are powerful instruments. In reference [112], the authors recorded for ten days the activities made by a subject utilising different typologies of sensors and devices, including a smart floor. Through such recordings, they created a dataset used by different works [113, 114] to design and test solutions to the problem of activity recognition. When fusing information coming from different sources, the identification possibilities can improve. Utilizing pressure sensors placed under a mattress and on the floor, authors of [115] created a system that measures sit-to-stand transfers, thus providing information about the mobility of the subject.

Chapter 2

Building the systems: BCG and SCG

This chapter focuses on discovering physiological parameters through BCG and SCG signals. The first part of the chapter describes the IoT acquisition system's behaviour and design; both its hardware and software parts are discussed. Successively, the focus is on the data analysis; the algorithm is explained through graphs and mathematical formulas. Different versions of the acquisition system and the algorithm for BCG/SCG analysis have already been published in the following papers: [51, 68, 45, 116, 117, 118, 119].

2.1 The acquisition system

Designing a system that provides physiological parameters requires a device to acquire the necessary waveforms. We have developed an IoT BCG and SCG acquisition device that senses acceleration signals. From the perspective of a future deployment in AAL scenarios, we designed the system through low-cost custom hardware. Even with low-cost hardware, our system could satisfy the necessities required by such a system; sensitivity and synchronisation constraints among all. Considering the limited amount of indispensable components (accelerometer, microcontroller, Wi-Fi

module), the overall cost of the acquisition device for future production can be relatively small, around fifty euros.

Utilising the acquisition system, we have acquired multiple datasets, over which we have tested and perfected our algorithm for physiological parameters detection.

The system evolved through time, and different modifications changed its behaviour and elements. The following paragraphs only describe the system's final design; other components used but not present in the last version are described only if necessary.

2.1.1   The behaviour of the system
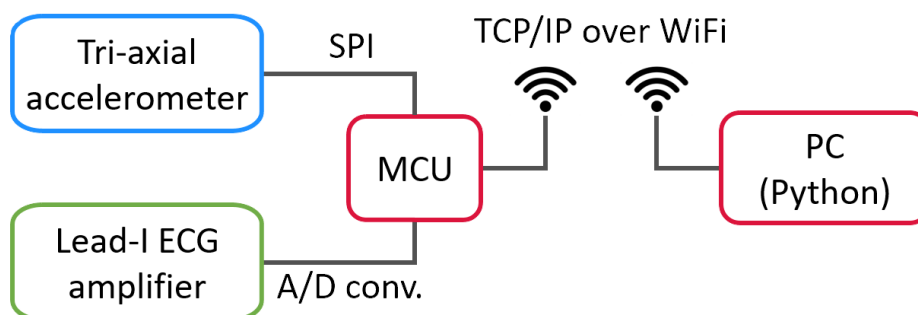
Figure 2.1: The block diagram of the acquisition system.

Figure 2.1 displays the block diagram of the acquisition system. A controller board mounting a MicroController Unit (MCU) synchronously acquires acceleration and ECG signals. The accelerometers communicate with the MCU through the SPI (Serial Peripheral Interface) protocol, whereas the ECG is obtained through an Analog-to-Digital Converter (ADC). Successively, the MCU streams the information through TCP/IP over a Wi-Fi connection to a receiving client. A desktop computer hosts the client and stores the data for further offline processing. This configuration allowed us to collect three over four of the datasets discussed in Chapter 4.

With accelerometric signals, we acquired a concurrent ECG. Its use is necessary

to have an evaluation tool to use for the algorithm's performance assessment; its use is restricted to that purpose only. While the system is used only in laboratory conditions, the ECG is necessary and not problematic. The ECG will no longer be part of the system for future usees in domestic environments.

For some measurements, we acquired signals from two different accelerometers; such signals are not part of the present work but will involve future studies. That is why there is a dotted accelerometer block in the diagram of Figure 2.1.

2.1.2 The elements of the system

The acquisition system contains different elements listed and explained in the following paragraphs. It is worth remembering that the design evolved through time. The main change of such evolution is using a different controller board. Some of the datasets were acquired through the initial controller board, while others through the final one. In Chapter 4, each dataset's description contains information about which board was used.

The controller boards

The primary duty of the controller board is to acquire the signals from sources, the accelerometers and the ADC. The first design of the system used an Arduino MKR1000 WiFi[1] as a controller board (Figure 2.2a). The successive design substituted such board with a more functional one, the B-L475E-IOT01A[2] (Figure 2.2b). Such choice was driven by higher performances and more friendly developments tools. The Arduino MKR1000 WiFi features:

- A SAMD21 Cortex®-M0+ 32bit low power ARM® MCU (ARMHoldings, Cambridge, England, UK).

- A 48 MHz clock and a Real-Time Clock (RTC) with a frequency of 32.768 kHz.

- Different 12-bit ADCs with up to 350 ksps.

---

[1] https://docs.arduino.cc/hardware/mkr-1000-wifi
[2] https://www.st.com/en/evaluation-tools/b-l475e-iot01a.html
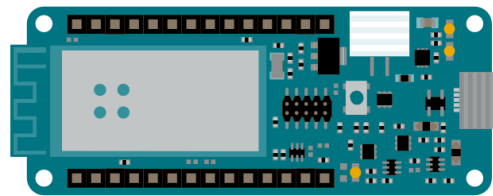
(a)
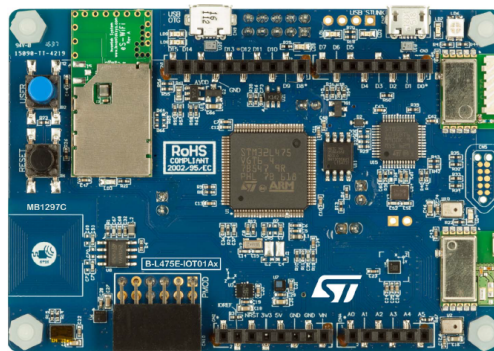
(b)

Figure 2.2: **(a)** Top view of the Arduino MKR1000 WiFi. **(b)** Top view of the B-L475E-IOT01A Discovery kit.

- An ATSAMW25 SoC from Microchip Technology Inc. for Wi-Fi connectivity.

- SPI, I^{2}C and UART peripherals.

- A 256KB Flash memory and a 32KB SRAM memory.

- Power saving features

Instead, the B-L475E-IOT01A features:

- An STM32L475VG MCU from STMicroelectronics with an ARM$^{®}$ Cortex$^{®}$-M4 32-bit.

- An 80 MHz clock and a 32 kHz crystal oscillator for RTC.

- Two fast 12-bit ADCs up to 5 Msps.

- An ISM43362-M3G-L44 module for Wi-Fi connection from Inventek Systems.

- Multiple SPI, I^{2}C and UART peripherals.

- A 1 MB Flash memory and a 128 KB SRAM memory.

- Power saving features

The ADXL355

(a)	(b)
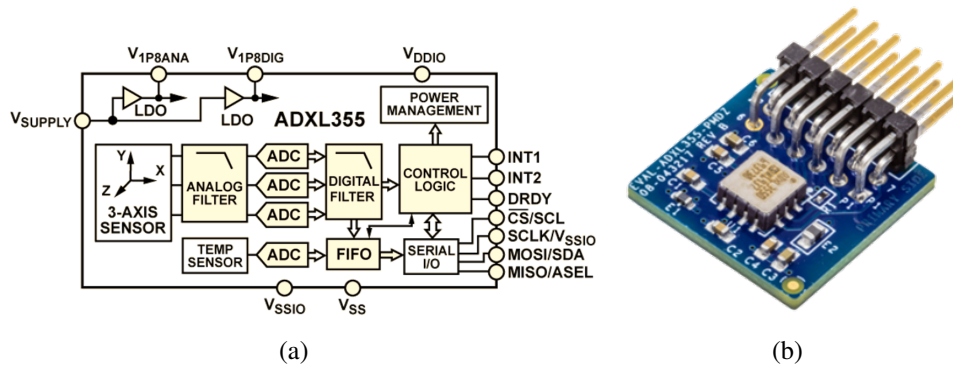
Figure 2.3: **(a)** The schematic of the ADXL355 accelerometer. **(b)** The top view of the ADXL355 evaluation board.

The ADXL355[3] accelerometer by Analog Devices, Inc. is the sensor that allows BCG and SCG signals acquisition. In particular, we used the EVAL-ADXL355-PMDZ evaluation board for our setup. Figures 2.3a and 2.3b show the block diagram of the accelerometer and the evaluation board, respectively. From Figure 2.3a is possible to see that the ADXL355 is a 3-Axis accelerometer; moreover, it is a MEMS (Micro Electro-Mechanical Systems) device that offers the following features:

- Zero g offset over temperature (0.15 mg/°C maximum) on all axes.

- Ultralow noise spectral density ($22.5\mu g/\sqrt{Hz}$) on all axes.

---

[3]https://www.analog.com/en/products/adxl355.html

- SPI and I^{2}C interfaces.

- 20 bit ADC.

- Programmable high-pass and low-pass digital filters.

- Selectable measurement range ±2g, ±4g, ±8g.

- Internal FIFO.

To sense the tiny vibrations produced by the heart movements or blood recoil forces, we programmed the accelerometer to work in the ±2g range to have the maximum possible resolution.

The AD8232 board
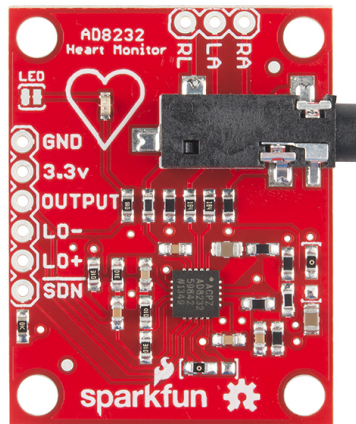
Figure 2.4: Top view of the AD8232.

We used Ag/AgCl electrodes and the AD8232[4] SparkFun single lead heart rate monitor board to acquire the ECG signals. Such board (Figure 2.4) mounts the AD8232 chip from Analog Devices Inc. and provides different useful features, like:

---

[4]https://www.sparkfun.com/products/12650

- An analog output.

- Left-arm, right-arm, and driven right leg pins to sense a Lead-I ECG and remove common-mode interference.

- 3.5mm Jack connection for cables plug-in.

- Leads-off detection to identify if an electrode is not correctly attached to the skin.

- Shutdown pin to switch off the device.

2.1.3 The sequence of operations
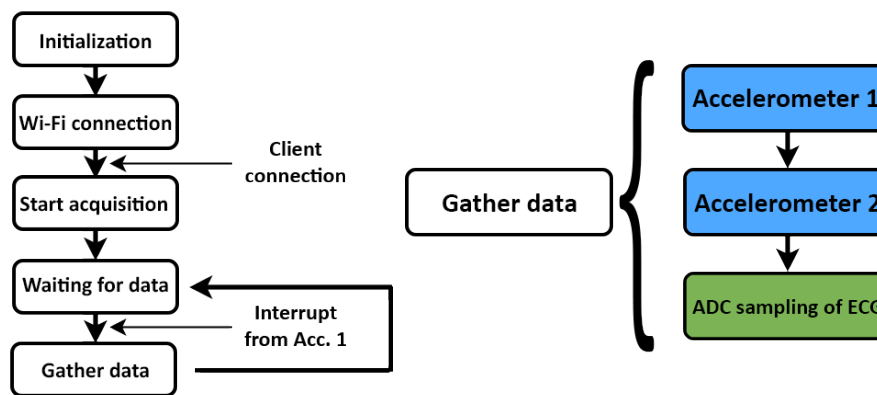
Figure 2.5: The sequence of operations of the acquisition system.

Figure 2.5 shows the sequence of operations that the controller board does to acquire the data. Firstly, all the devices and peripherals are initialised. Secondly, the controller board starts the Wi-Fi connection and waits for a client to connect (the controller board act as a server). At the client connection, the controller board starts the data acquisition from the accelerometers.

The ADXL355 can provide a data-ready signal which informs that a successful sampling is concluded. Such signal is used as an interrupt by the MCU and schedules all the devices' sampling instants. Whenever the data-ready signal alert that a successful conversion has happened, the MCU gathers the data from all the accelerometers and starts an ADC sampling of the ECG signal. The sampling frequency of the ADXL355 can be selected through proper programming.

The signals acquisition is executed in sequence; the accelerometer that has generated the data-ready signal is the first. Next comes the other accelerometer (if present) and the ECG signal. A sequential acquisition causes two problems:

1. The accelerometer and the ECG are sampled in two different instants.

2. The second accelerometer accumulates a delay because the accelerometers are inside two different evaluation boards, with two different oscillators which have slightly different frequencies. Such delay implies duplicating a sample with a frequency that depends on the oscillator frequencies' difference.

Due to the conversion speed of the ADC inside the B-L475E-IOT01A, the first problem is negligible, and the signals can be considered simultaneous. Even in the case of less fast ADC conversions, such delay is constant and can thus be removed in the processing phase.

The second problem can be resolved by doubling the frequency of the additional accelerometer. In this way is assured that for each sample provided by accelerometer one, there will always be a new sample provided by accelerometer two. This solution implies an increase in power usage.

After acquiring a certain quantity of data, the controller board sends them to the client and continues the acquisition. When the client has obtained sufficient data, it sends a transmission end message, and the connection stops. Finally, the controller board brings itself to the client's waiting condition.

The acquisition software
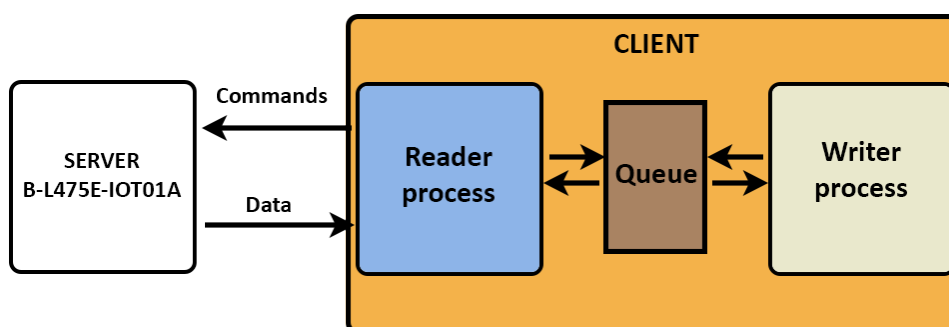
Figure 2.6: The elements of the acquisition software.

The software that acquires the data stream and saves it into a hard drive runs in a Python[5] environment over a personal computer that acts as a client.

Figure 2.6 shows the different elements of the software: two processes and a queue. The two processes are named reader and writer; the queue allows the exchange of information between them. The reader process has the duty of collecting the data sent by the controller board and starting and stopping the acquisition. Through the queue, the data are transferred to the writer process, which orders the data and saves them in an HDF5[6] (Hierarchical Data Format) file on the hard drive. By changing a parameter in the software, the program adjusts the acquisition duration. The client sends an end message to the controller board through the reader process when the total acquisition time elapses. Successively, the HDF5 file is closed as the queue, and the processes stop executing.

---

[5]https://www.python.org/

[6]https://www.hdfgroup.org/

2.2 Waveforms analysis

The purpose of the proposed methodology is not to substitute medical devices or diagnose illnesses; the system designed aims to identify abnormal patterns from physiological measures protracted in time (for months or even years). Such an approach can be especially beneficial to the fragile subjects and their caregivers, which can use such identifications to prevent undesired conditions.

Our methodology aims to identify heartbeats and estimate cardiac cycles. We reached such goals by assuming a regular heartbeat in the subjects under test. We can obtain precise HR and HRV indicators through our methods, which allow us to monitor and possibly detect anomalous trends.

To extract physiological information from the BCG and SCG signals, it is essential to detect the positions of the heartbeats. The Pan–Tompkins algorithm [33] is a well-established technique for identifying the R-peaks positions inside the ECG, thus identifying the heartbeats. Instead, SCG and BCG segmentation methods have recently been proposed in the literature [120, 121]. However, the literature lacks a unified approach to analyse and segment SCG and BCG to the best of our knowledge; the following paragraphs describe our attempt to achieve it. Such methodology was already presented in [68].

2.2.1 Data pre-processing

The ECG and the BCG/SCG waveforms were initially pre-processed to obtain a more easy annotation. First, a bandpass FIR (Finite Impulse Response) filter is used on both BCG/SCG and ECG. Pass-bands of [0.5 Hz - 45 Hz] and [2 Hz - 14 Hz] range were used for ECG and BCG/SCG, respectively. We used zero-phase digital filtering to maintain a correct alignment between BCG/SCG and ECG signals. Since the ECG is used only for reference purposes, the bandwidth chosen is sufficient to show the R-peaks in the signal, thus the heartbeats position. The BCG and SCG bandwidth was selected because most of the information is contained within such intervals [122, 123].

One of the databases analysed in Chapter 4 was downloaded from a public repos-

itory. The dataset was sampled at 5 kHz, a frequency excessively high to be analysed easily. We downsampled this dataset only down to 500 Hz.

The second and final pre-processing step was normalization through z-scoring:

$$s_{zsc} = \frac{s - \mu_s}{\sigma_s},$$

(2.1)

where s is the signal of interest, μ_s is its mean, σ_s is its standard deviation and s_{zsc} is the z-scored signal.

2.2.2 The algorithm for heartbeats identification
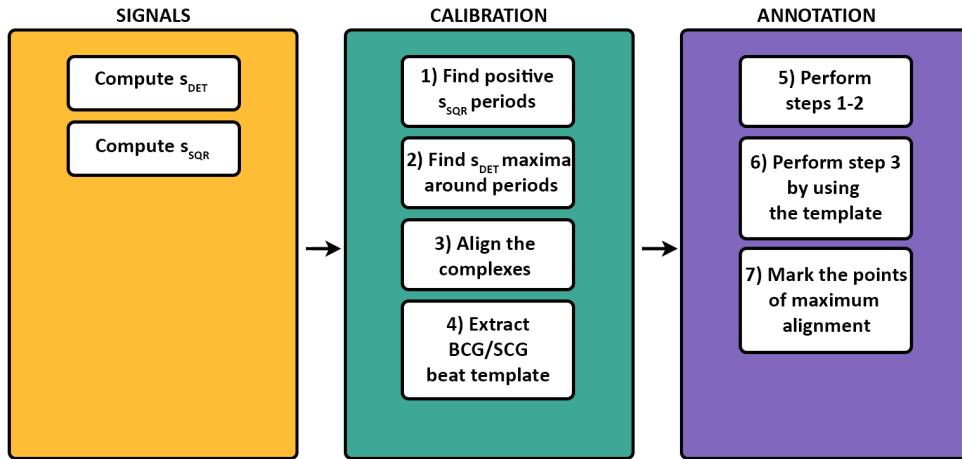
Figure 2.7: The various steps of the annotation algorithm, divided by phase.

Many physiological and anatomical factors contribute to the oscillatory complex of the SCG or BCG heartbeat. Therefore, accurate heartbeat pattern identification can be challenging without prior knowledge or references. However, indications come from the energy inside BCG/SCG data. Thus, initially, the algorithm identifies potential locations of the BCG/SCG complexes through inspection of the signal energy. Indeed, such energy increases around the areas of the heartbeats. The algorithm proposed utilises a detection signal (s_{DET}) to identify such energy increases, defined as follows:

$$s_{DET}[n] = \sum_{k=0}^{M-1} b[k] \cdot s_{zsc}^2[n-k], \qquad (2.2)$$

where s_{zsc} is the preprocessed BCG/SCG signal and $b[k]$, $k = 0, ..., M-1$ are the coefficients of a low-pass FIR filter. We used $M = 256$, and a cutoff frequency of 2 Hz.

To refine the segmentation and better identify the zones of high signal energy, the s_{DET} waveform is processed using a sliding-window filter, which is defined as follows:

$$s_{SQR}(i) = \begin{cases} 1, & \text{if } s_{DET}(i) \geq \mu_{i:i-p} + k \cdot \sigma_{i:i-p} \\ -1, & \text{otherwise} \end{cases}, \qquad (2.3)$$

$\mu_{i:i-p}$ is the average of the last p points ($p = 4\,\text{ms} \cdot 30/T_s$, where T_s is the sampling interval), $\sigma_{i:i-p}$ is the standard deviation over the last p points, and k is a multiplication factor that determines the level over which the sample must be to have a positive output. If k is too high, it can bring to skipping potential heartbeats. Contrary, if the value of k is too low, it is easier to discover energy variations, including the ones not related to a heartbeat. To choose the best value of k possible, we have conducted a parametric sweep over the performance metrics; the results showed that $k = 2$ is the optimum value.

The positive intervals of the signal s_{SQR} determine the candidate heartbeats positions. Within such zones, the s_{DET} signal is inspected, and its local maximum is annotated. Such points are used as approximated locations for the heartbeats. In case the time interval between two maxima is considered too wide, the research of heartbeat energy is performed again, with a reduced value of the parameter k in equation 2.3. The time intervals are considered unacceptable if their value exceeds 1500 ms, corresponding to an HR of 40 beats per minute. The research is performed gain even if the relative variation between two successive intervals is higher than 30%.

After detecting enough candidate heartbeats, the calibration phase starts. Such a procedure creates a heartbeat prototype through the alignment of successive beats. The purpose of such a phase is to personalise the algorithm and adapt it to the unique
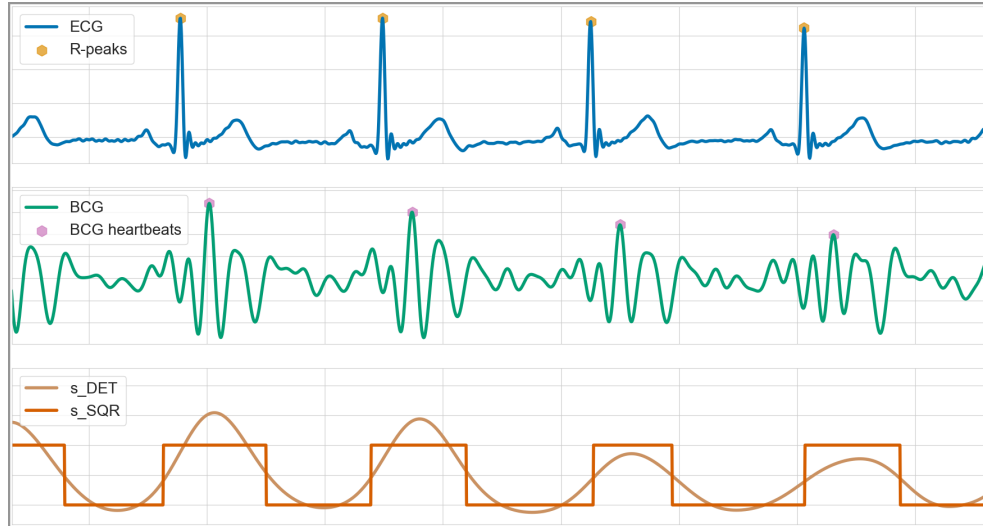
Figure 2.8: The various waveforms used for heartbeats identification and evaluation.

heartbeat pattern of the subject. Portions of the BCG/SCG signal, centered in the s_{DET} maxima, are taken and aligned with each other through a gradual shift, trying to maximise their cross-correlation. The shifting is limited to a delay of $\pm\tau_S = \pm 200$ ms from the s_{DET} maxima. The template $s_{zsc,T}$ is extracted from the signals aligned by computing the median; such a procedure involves only the first 20 candidate heartbeats.

The annotation phase directly follows the calibration phase. Starting from the positive intervals of signal s_{SQR}, the extracted prototype is cross-correlated with the BCG/SCG signal, and the points of maximum correlation are annotated. Such points are the algorithm's output and represent the heartbeats inside the BCG/SCG trace.

The entire procedure is shown graphically in Figure 2.7. It is divided into three main blocks: in the yellow one there is the computation of the signals; the light blue one represents the calibration procedure; lastly, the purple one is the annotation phase. Instead, Figure 2.8 shows the waveforms used for annotation and evaluation of a BCG recording. The middle panel shows the BCG signal in green and the marks identified using the algorithm in pink. The low panel shows the s_{DET} waveform in

brown and the s_{SQR} waveform in orange. The top panel shows the ECG signal in blue with the R-peaks marked in yellow; it is worth reminding that the ECG is used only for evaluation purposes and is not used by the annotation algorithm.

Chapter 3

Building the systems: the smart floor

Stimulating and educating people to have active behaviours during their lives is challenging because it has to influence people's nature and beliefs. It is not possible to force someone to have an active life, but creating objects that stimulate such behaviour can positively impact. For this reason, a smart floor can be a device suitable for the cause. Indeed, a smart floor can provide entertainment, active interaction and valuable services (especially in a domestic environment). Furthermore, it can be an inter-generational device that can be used by grandparents and grandsons together.

This chapter presents the study and the development of an IoT smart floor. Initially, it provides a broad view of the system behaviour and its main components. Successively, the discussion focused on each part of the smart floor, presenting the main characteristics and the problems which drove some choices.

The smart floor is one element of a larger project called PLEINAIR (Parchi Liberi E Inclusivi in Network per Attività Intergenerazionale Ricreativa e fisica), funded by Regione Emilia Romagna. We designed other objects for it, particularly a smart table and a smart bench. Such devices share with the smart floor their principal component, the smart tile. Because the technology is the same for all the objects, to avoid redundancy the discussion focus only on the smart floor, the most complicated one.

3.1   The behaviour of the system

The smart floor is created by combining various smart tiles, which can interact with the users through piezoresistive sensors and luminous feedback. The smart floor uses such qualities to instruct the users on the actions to do during the game execution and to record mistakes or the correct movements. A web app provides information and control of the desired game while also showing the user's scores at the game end. Both luminous feedback and scores can engage the user, thus stimulating active behaviour. One of the user's controls over the game is its difficulty; with such an option, the game's enjoyment can be adapted to the subject, thus increasing the personalisation and stimulation.

Even though the typologies of inputs and outputs are a few, multiple games can be created upon the smart floor, limited only by imagination. The game described in this document is the molten floor game. To complete the game successfully, the players must follow the path indicated by the green tiles and avoid touching the ones turned off. The faster the completion, the higher the score.

Figure 3.1 shows the sequence of operations that the users can do to interact with the smart floor; it also provides a summary picture of the molten floor game.
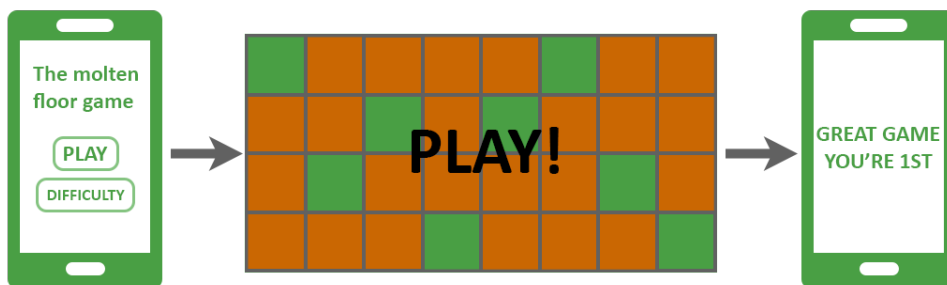
Figure 3.1: The users can interact with the smart floor through a web-app that allows control and provide the results at the end of the game.

3.1.1 The elements of the system
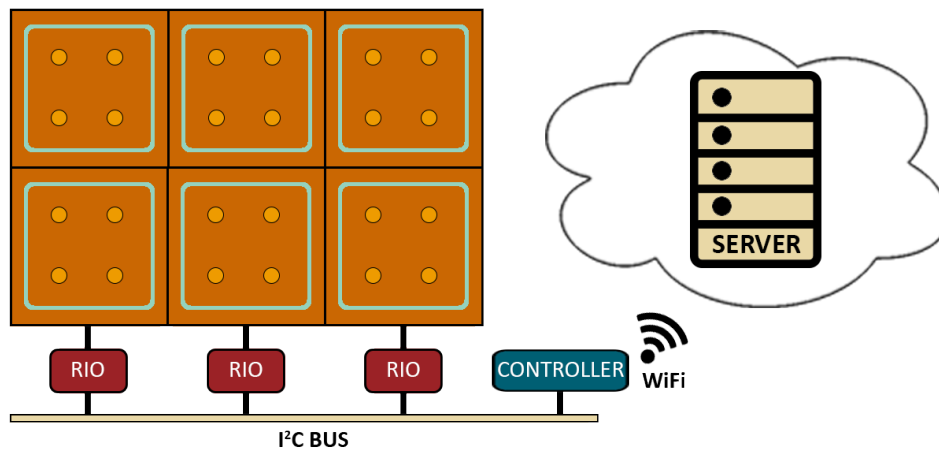
Figure 3.2: View of the elements of the smart floor system. The RIO modules and the controller board control the smart floor system. All the boards communicate with each other over an I^{2}C (Inter Integrated Circuit) bus. After an elaboration phase, the controller board transmits the data to a server through Wi-Fi. The elements' dimensions are out of scale for better understanding.

Figure 3.2 shows the different elements of the smart floor system; each one has a different colour:

- The tiles are represented as brown squares.

- The piezoresistive sensors are the yellow circles.

- The LED strips are light blue squares.

- The Remote Input Output (RIO) boards are the red squares.

- The controller board is a blue square.

- The I^{2}C bus is the white line.

A total of 32 tiles were used to create the smart floor. Each tile is a square of 50 cm, while the smart floor is 4 meters large and two meters long, for a total of 8 m^2. Figure 3.2 shows only a portion of the floor.

Even if present in Figure 3.1.1 for clarity purposes, the server was not part of the present work (both back-end and front-end) and its control was implemented by DataRiver S.r.l., one of the partners of the PLEINAIR project.

Costs reduction was not the main focus during the development; indeed, the overall cost of the elements of one smart tile was around 800 euros. Such a price is acceptable for an early-stage device, but it is not for a product addressed to the consumer. For future commercialization, those smart devices must reduce their price by acting over the mechanical structure and the electronic circuits.

3.1.2 System requirements

The smart floor must be an enjoyable instrument to stimulate the user to have active behaviour. The interaction needs to be responsive to reach such a purpose. A responsive system can quickly identify the users' actions and immediately provide the outputs.

The 300 grams constraint

The possible users' actions depend upon the typologies of the sensors and the electronic circuits which control them (more on the electronic circuits and the choice of the sensors in sections 3.2.2 and 3.2.1, respectively). The smart tiles were equipped with piezoresistive sensors, devices able to sense the pressure applied to them. Such property means that a smart tile can identify a weight present above them or a weight change, like when a person steps on or steps off it.

To quickly identify a pressure change, the smart tile must be sensitive to tiny variations. The system was designed to detect a 300 grams mass presence above each tile. Identifying 300 grams allows quickly detecting the pressures impressed by a child or by a hand instead of a foot. The inter-generational quality that the system aspires to have had influenced this choice. Experimental measures tested the mechanical struc-

ture of the tile and the sensors to assess the sensitivity requested (section 4.2.1discuss the results of such tests).

A quick reaction of the system

With a fast identification of a user's action, the smart floor can provide a quick output. The rapid response requirement is ensured by a Microcontroller Unit (MCU) which equip both the controller and the RIO boards. The MCU allows to measure the events above the floor with a precision of 10 ms and inform the controller board immediately after the detection. The I^2C bus is the platform that allows communication to happen (section 3.2.4 provides more information on the communication between the boards). When the controller board receives the message, it chooses how to react and informs the RIO boards that control the luminous outputs. LEDs strips provide such outputs with different colours and visual effects. The entire communication happens fast so that the user perceives an immediate response by the system to its actions.

3.1.3   The sequence of operations
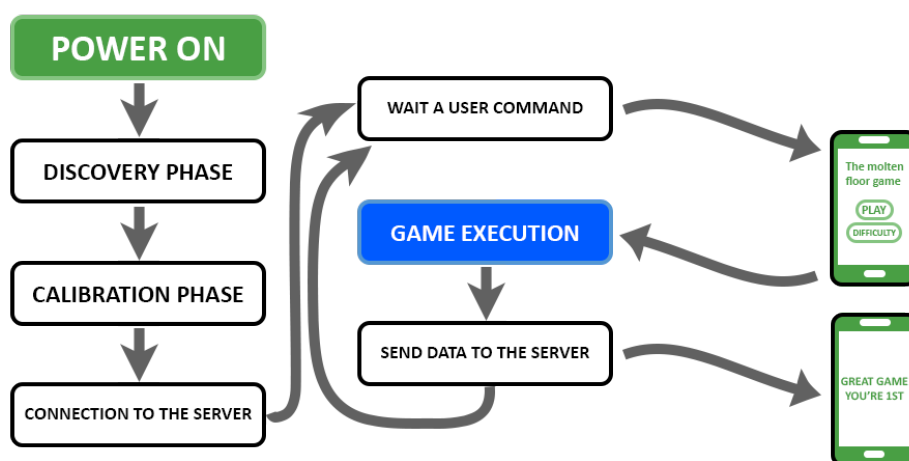
Figure 3.3: The sequence of operations that the smart floor does while powered on.

Figure 3.3 shows the sequence of operations that the system computes at its startup. The following list gives an overview of each phase:

- Discovery phase: the parameters used for correct communications between the electronic boards are initialised.

- Calibration phase: the circuits which allow the sensors to function are properly calibrated.

- Connection to the server: the controller board starts the Wi-Fi connection and connects to an access point. Successively, the board connects to the server.

- Wait for a user command: the system enters this phase after connecting to the server and after data transmission. Nothing happens inside this phase; the system waits for a user command.

- Game execution: during this phase, the user can play the game selected at the chosen difficulty. This phase starts when the user selects the game through the web app (represented by the smartphone in Figure 3.3).

- Send data to the server: at the game end, the controller board sends all the data gathered to the server, which elaborates and provides the results through the web app.

The sequence of phases is equal at each power on, but the execution of the discovery phase is different between the first startup and the successive. Because the changes happen inside such phase, the discussion about the differences is made inside section 3.2.4, which treats the communication infrastructure and procedures.

3.2   A deep discussion of the main elements

In the following sections, each element of the system is discussed in depth: section 3.2.1 presents the mechanical structure of the smart tile; section 3.2.2 discusses the RIO board; section 3.2.3 describes the controller board; section 3.2.4 illustrates the

setup procedures and the communications which allow the smart floor to operate; the topic of communications continues in section 3.2.5, where are described the Wi-Fi transmissions and the MQTT (Message Queue Telemetry Transport) protocol; finally, section 3.2.6 explains the algorithm structure behind the games.

3.2.1 Mechanical structure
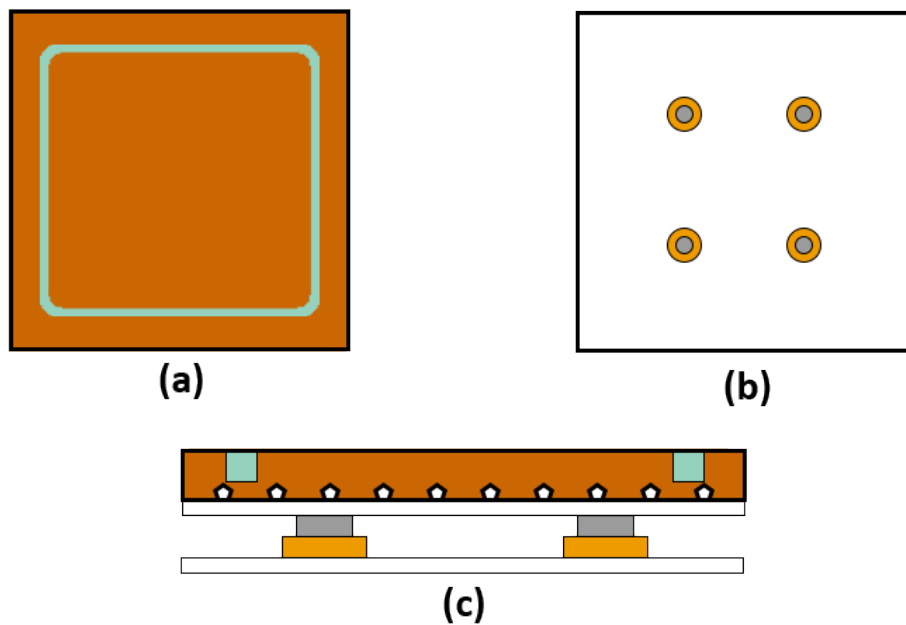
Figure 3.4: (**a**) Top view of the smart tile: anti-trauma tile and LED strip. (**b**) Top view of the bottom part of the smart tile: PVC layer, piezoresistive sensors and washers. (**c**) Lateral view of the smart tile. The top and bottom parts are put together while adding another PVC layer in between. The elements' dimensions are out of scale for better understanding.

We created the smart tile through the join of a top and a bottom section. Inside Figure 3.4 are shown different views of the smart tile and its parts. Figure 3.4a is the

top section, whereas Figure 3.4b is the bottom one. Instead, Figure 3.4c shows the lateral view of the smart tile in its entirety. In the figures, the brown parts represent the anti-trauma tile, the light blue colour is used for the LED strips, the white rectangles are PVC (PolyVinyl Chloride) layers, the yellow and grey elements are the piezoresistive sensors and washers, respectively. The design of the device took into consideration both indoor and outdoor contexts, for this reason, the material used for the floor is anti-trauma, which is typically used in playground environments to avoid injuries and hurts.

The white pentagons in Figure 3.4c represent the not uniform texture that the anti-trauma tile has at its bottom surface. Due to such texture, the pressure tends to focus on limited areas. Moreover, even the density of the tile is not uniform; thus, a weight applied in different zones of the tile transmits different pressures. The PVC sheet between the top and bottom sections is used to respond to such problems. Indeed, the PVC sheet allows the distribution of the forces above the sensors. Even the use of washers allows concentrating the force above the sensors. Instead, the bottom PVC sheet provides a solid and smooth basement that supports the entire structure.

The mechanical design looked for a simple structure and high sensitivity to little pressures. Joining those requirements brought some challenges, like choosing the suitable typology of sensors. Load cells, piezoelectric sensors and piezoresistive sensors were considered. The necessity for a dedicated and complex mechanical structure to obtain a suitable coupling discarded the load cells. Instead, without specific algorithms or dedicated electronics, piezoelectric sensors cannot identify a stable weight. Thus, we choose piezoresistive sensors because they can sense stable weights with a proper and simple signal conditioning circuit and they can be mounted easily. We chosed the Flexiforce^{TM} A201 by Tekscan^{TM} as the sensing element. Such a device has a broad force range and has small dimensions (a thickness of only 0.203 mm). Both its resistance and resistance variation reduce with the increase of the pressure applied.

The position and quantity of sensors to use on each tile was a design issue that required a deep exploration. The Flexiforce^{TM} A201 has a small sensing area (a circle of 9.53 millimetres in diameter); thus, using only one sensor does not allow to have

the desired sensitivity in the entire tile. Experimental measures discovered the best quantity of sensors to place under the tile. Section 4.2.1 discusses the results of the experimental measures, which suggest that four sensors can fulfill the requirements.

The uneven density of the anti-trauma tile brought a problem in the conditioning circuit of the sensors. Indeed, a different and unpredictable distribution of the weight over the sensors implies different resistance values. Such variation forced us to design a dynamic conditioning circuit to adapt to every resistance value. The resistance span reduces thanks to the PVC sheet, but this decrease is insufficient to have a unique polarisation circuit. Section 3.2.2 explains the solution we have designed.

3.2.2 Remote Input Output board
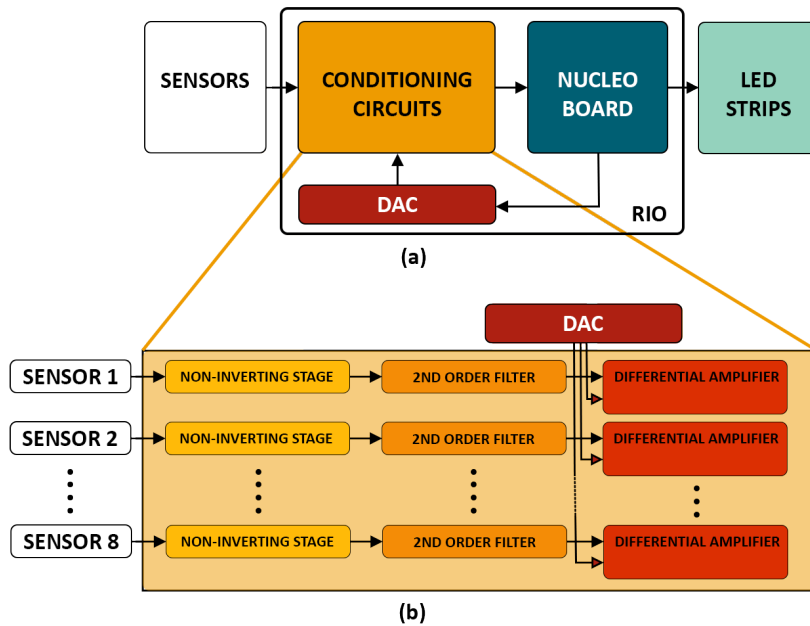
Figure 3.5: (**a**) Block diagram of the electronic circuit of the RIO boards. (**b**) The stages of the conditioning circuit.

The RIO board was engineered for the smart floor; Figure 3.5a shows its block di-

agram of elements and connections. The sensors connect to the conditioning circuits that provide output signals to a NUCLEO-L432KC board from STMicroelectronics, which mounts a STM32L432KCU6U MCU. The LED strips are controlled through Pulse-Width Modulation (PWM) by the NUCLEO board. An analog to digital converter (ADC) integrated inside the NUCLEO board sample the outputs. During the calibration phase, the microcontroller processes the samples to pilot a multi-channel Digital-to-Analog Converter (DAC). The DAC outputs influence the conditioning circuits; their voltage values depend on the resistance of the respective sensor.

The entire smart floor use sixteen RIO modules, because one board can sense eight different sensors and control two LED strips, the elements of two tiles. A 3.3 V LDO (Low-DropOut) regulator embedded into the NUCLEO-L432KC board power both DAC and conditioning circuits; instead, an external 5 V source powers the LED strips, which mount the WS2812B LED controller by Worldsemi. A photograph of the RIO board is visible in Figure 3.6.
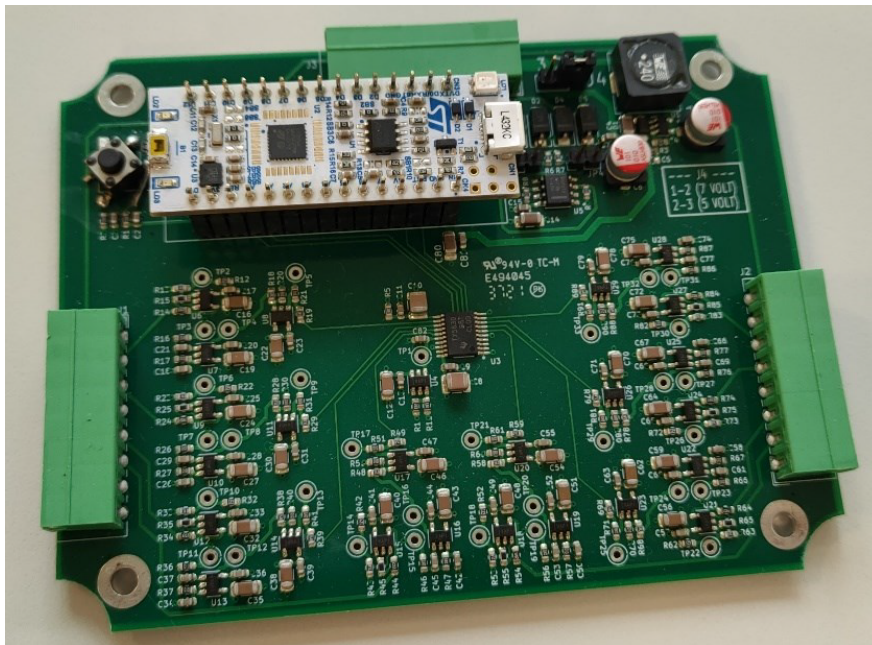
Figure 3.6: The RIO board.

The conditioning circuit

Figure 3.5b shows the conditioning circuit and its main blocks necessary to control one sensor, eight of them are inside one RIO board. The following list explains the function of each stage:

- The first stage is a non-inverting amplifier that amplifies a fixed voltage; the sensor resistance changes the value of the amplification.

- The second stage is a second-order Sallen-Key filter which removes the power line interference.

- The third stage is a differential amplifier used to amplify the difference between the second stage output and the output of the DAC.

Through the use of a DAC, we solved the problem of the difference between the initial values of the sensors. The DAC allows personalising the circuit to each piezoresistive sensor, and to settle the output of each conditioning circuit around the same voltage.
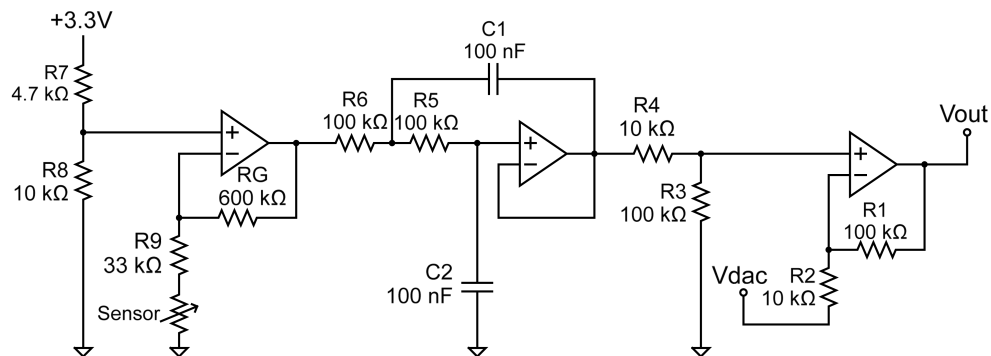
Figure 3.7: The schematic of one conditioning circuit.

Figure 3.7 shows the schematic of the conditioning circuit. The DAC tension subtracts the output of the second stage, which is controlled by the sensor resistance; thus, an increase in the DAC output produces a lower voltage at the conditioning circuits output. During the calibration phase, when the tiles do not have any weight

above them, the DAC values are changed to equal the voltages of the different second stages and to provide zero volts outputs. During the game execution, pressure will create a difference between the inputs of the differential amplifier (the one on the right of Figure 3.7), which will increase the output voltage. Thanks to such a circuit, the system can identify even the touch of a hand.

The operational amplifier used in the conditioning circuit is the OPA2340[1] from Texas Instruments, an input and output rail-to-rail CMOS device. The features which led to its choice are:

- The input offset voltage is driven by the power supply (PSRR) of 120 μV/°C.

- The input bias current of ± 0.2 pA.

- The input offset current of ± 0.2 pA.

- High differential and common-mode input impedance.

Significant for the project is the PSRR (Power Supply Rejection Ratio) characteristic that allows the device to be unaffected by the switching inside the boost circuit, which powers the RIO board.

Mathematical description of the conditioning circuit

The following equations explain the behaviour of the conditioning circuit in a mathematical language and refer to Figure 3.8a where the second-order filter has been removed for better clarity purposes.

$$V_X = V_{CC} \cdot \frac{R_7}{R_7 + R_8} \tag{3.1}$$

$$V_1 = V_X \cdot (1 + \frac{R_G}{R_9 + R_S}) \tag{3.2}$$

$$V_Y = V_1 \cdot \frac{R_3}{R_3 + R_4} \tag{3.3}$$

---

[1]https://www.ti.com/lit/ds/symlink/opa2340.pdf
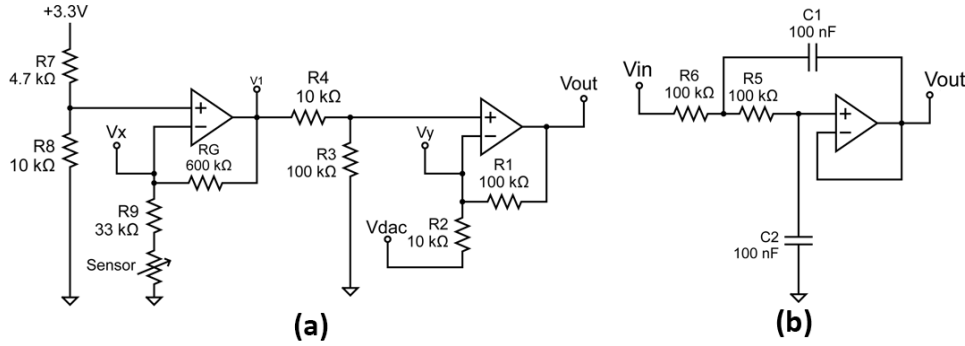
Figure 3.8: **(a)** The first and third stages of the conditioning circuit, without the second-order filter. **(b)** The second-order filter.

$$V_{OUT} = V_Y + \frac{R_1}{R_2} \cdot (V_Y - V_{DAC}) \tag{3.4}$$

Where RS is the sensor resistance, V_{CC} is the power supply, V_X and V_Y are the voltages at the operational amplifier's negative inputs, and V_1 and V_{OUT} are their output voltages, as Figure 3.8a shows.

Instead, equations 3.5 and 3.6 explain the second-order filter behaviour (Figure 3.8b).

$$H(s) = \frac{1}{1 + C_2 \cdot (R_6 + R_5)s + C_1 C_2 R_6 R_5 s^2} \tag{3.5}$$

$$F_c = \frac{1}{2\pi \cdot \sqrt{R_6 R_5 C_1 C_2}} \tag{3.6}$$

Where $H(s)$ is the filter's transfer function and F_c is its cutoff frequency. Replacing resistances and capacitors of equation 3.6 with the values written in Figure 3.8b gives a cutoff frequency value of:

$$F_c = 15.92 \ Hz$$

The response of the conditioning circuit

Figure 3.9 shows a simulation of the circuit's response, which illustrates the changes in the output voltage due to a variation in the sensor resistance. The image also shows
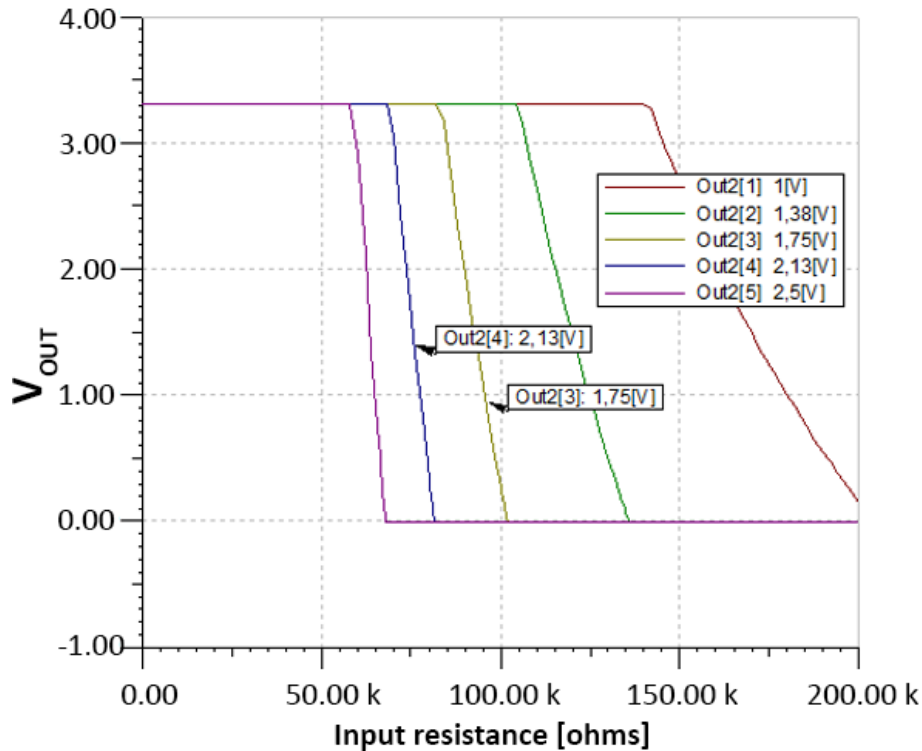
Figure 3.9: The simulation of the conditioning circuit's response. Each curve displayed has a different value of the DAC voltage.

how the response changes when a different DAC voltage is used to polarise the conditioning circuit. Each curve has three stages, a top and a bottom saturation stage and a gain stage. During the calibration phase, the DAC voltages are adjusted to bring the outputs of all the conditioning circuits to the bottom knee of the curve. At such a point, the circuit has the maximum sensitivity; indeed, a little pressure above the tile brings the circuit to the gain stage and an output voltage increase.

Figure 3.9 shows an undesired effect brought by the solution adopted; the slope of the different curves changes with the value of the DAC voltage. In particular, the higher the voltage, the higher the gain. Such behaviour should have brought a higher sensitivity to the more polarised sensors; this does not happen because of the inverse

proportion between resistance variation and force applied. Indeed, a sensor with high pressure applied changes its resistance less than one with low pressure. Such an effect counterbalance the change in gain.

Digital to Analog Converter

The Digital to Analog Converter is a TLV5630 [2] chip by Texas Instruments; it has eight output channels with a voltage resolution of 12 bits. The outputs can change in a few microseconds; how fast depends on the device's configuration. To interact with the device, the RIO uses the SPI (Serial Peripheral Interface) protocol, which allows configuring the device as desired by the user. An internal rail-to-rail amplifier buffers each output to provide enough current to the load without interfering with the correct behaviour of the DAC.

NUCLEO-L432KC
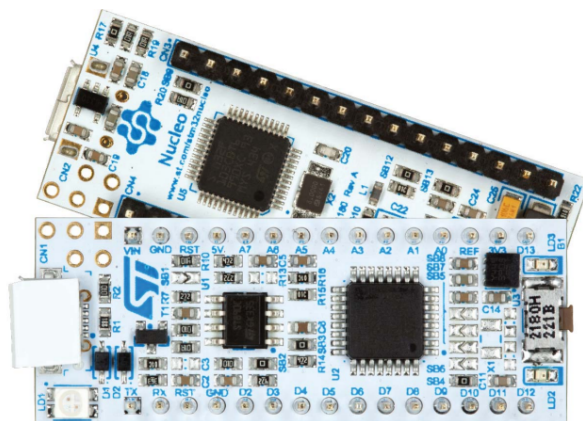
Figure 3.10: The NUCLEO-L432KC from STMicroelectronics.

The NUCLEO-L432KC [3] is a development board equipped with an STM32L4 family MCU based on Arm® Cortex®-M4 32-bit architecture. The microcontroller

---

[2]https://www.ti.com/lit/ds/symlink/tlv5630.pdf
[3]https://www.st.com/en/evaluation-tools/nucleo-l432kc.html

unit contains different peripherals which allow commanding two smart tiles; some of them are described in the following list:

- The Analog to Digital Converter (ADC) samples different channels attached to the conditioning circuit's outputs. The channels are multiplexed and sampled in sequence.

- By generating PWM signals, the Timers control the LED strips.

- With the I^2C communication interface, the RIO board can communicate with the other electronic boards of the smart floor.

- The SPI communication interface allows the NUCLEO to command the DAC outputs to control the conditioning circuit polarisation.

Power section
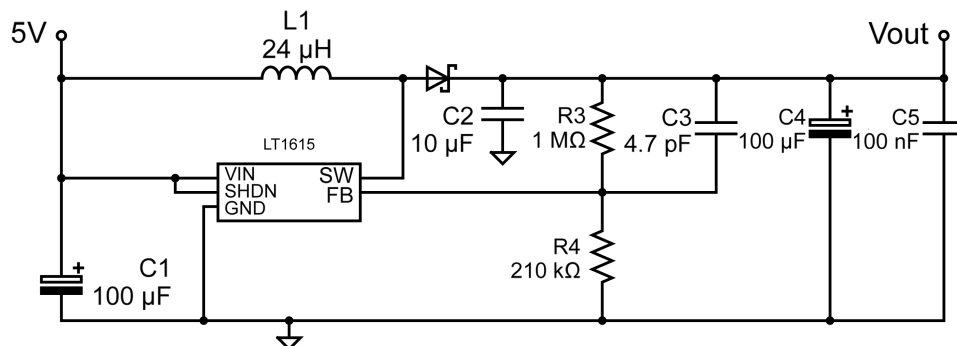
Figure 3.11: The power circuit of the RIO board.

The NUCLEO-L432KC is not allowed to be powered by a 5 volts supply unless by unsolder some bridges. Instead, a 7 volts (or greater) supply is permitted without any changes. Because the operation of unsoldering must be precise and repeated for each NUCLEO board used, the project choice was to design a boost circuit that provides a 7 volts supply. Figure 3.11 shows the boost circuit designed, where $5V$ is the power supply input, and V_{OUT} is the boost output that powers the NUCLEO board.

The DC/DC converter used is the LT1615[4] by Linear Technology, which can provide a current up to 350 mA. The 7 volts supply powers only the NUCLEO board; the other chips of the RIO board are powered by a 3.3 volts power supply provided by an LDO inside the NUCLEO board. Finally, the 5 volts power supply also powers the LED strips.

The I^{2}C bus extender
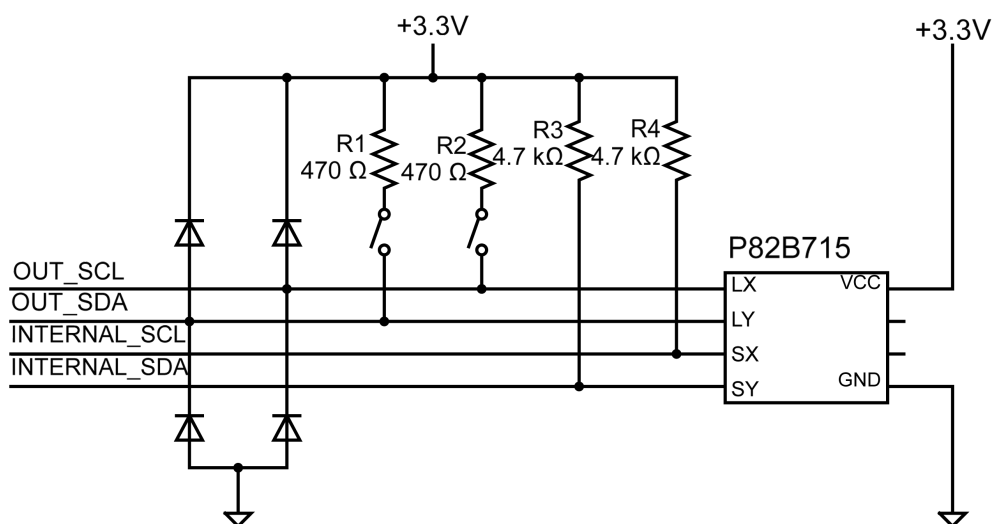
Figure 3.12: The I^{2}C bus extender circuit, with the P82B715 chip.

Over the I^{2}C bus the RIO boards and the controller exchange their information. Because I^{2}C is a collision avoidance protocol, it suits the system's necessity well. Indeed, two boards may try a simultaneous transmission over the bus, thanks to the collision avoidance feature such event is automatically resolved. The dimensions of the smart floor imposed to equip each board with an I^{2}C bus extender, the P82B715[5] from NXP Semiconductors. Figure 3.12 shows the circuit that connects the RIO with the I^{2}C bus; *OUT_SCL* and *OUT_SDA* are the connections to the

[4]https://www.analog.com/media/en/technical-documentation/data-sheets/16151fas.pdf
[5]https://www.nxp.com/docs/en/data-sheet/P82B715.pdf

bus lines, *INTERNAL_SCL* and *INTERNAL_SDA* are the connections with the NU-CLEO board. The external lines are protected by ElectroStatic Discharge (ESD) by two couples of diodes. The internal lines are connected to the 3.3 volts supply by pull-up resistors. Instead, the external lines connect to 470 ohms resistances through a couple of jumpers. The pull-up at the external lines is used only in the first and last board attached to the bus; thus, the internal ones must be free to disconnect the resistances. The total line capacitance was kept below 3000 pF using suitable connectors and proper cables, as suggested by the P82B715 datasheet.

3.2.3   The controller board
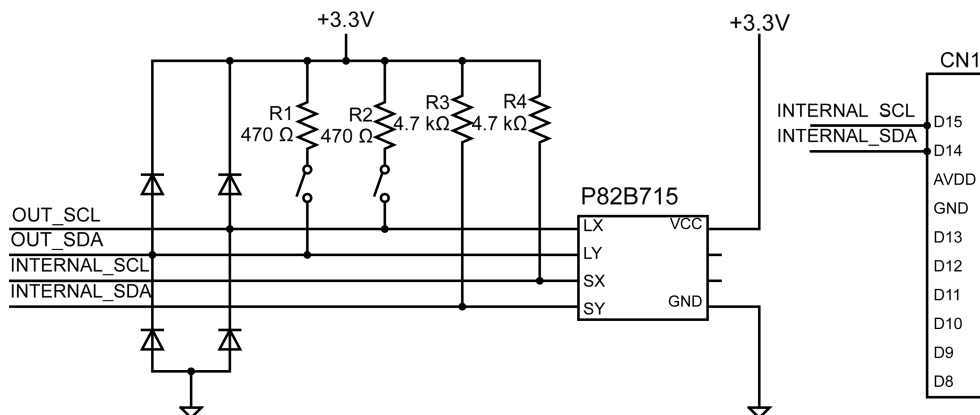
Figure 3.13: The connections between the B-L475E-IOT01A and the P82B715 bus extender.

One of the controller board elements is the B-L475E-IOT01A[6] Discovery kit from STMicroelectronics (Figure 2.2b), which has an STM32L4 series microcontroller based on Arm® Cortex® M4 processor and an ISM43362-M3G-L44 chip by Inventek systems for Wi-Fi connectivity. The circuits necessary for the controller to work were created in a matrix board; such board connects to the B-L475E-IOT01A. As for the RIO boards, also for the controller was used an I²C bus extender. Fig-

---

[6]https://www.st.com/en/evaluation-tools/b-l475e-iot01a.html

ure 3.13 shows the connections between the P82B715 chip and the CN1 connector of the B-L475E-IOT01A. Other circuit elements not represented in the figure are connectors and jumpers for the power supply.

3.2.4   The setup procedures

The discovery phase
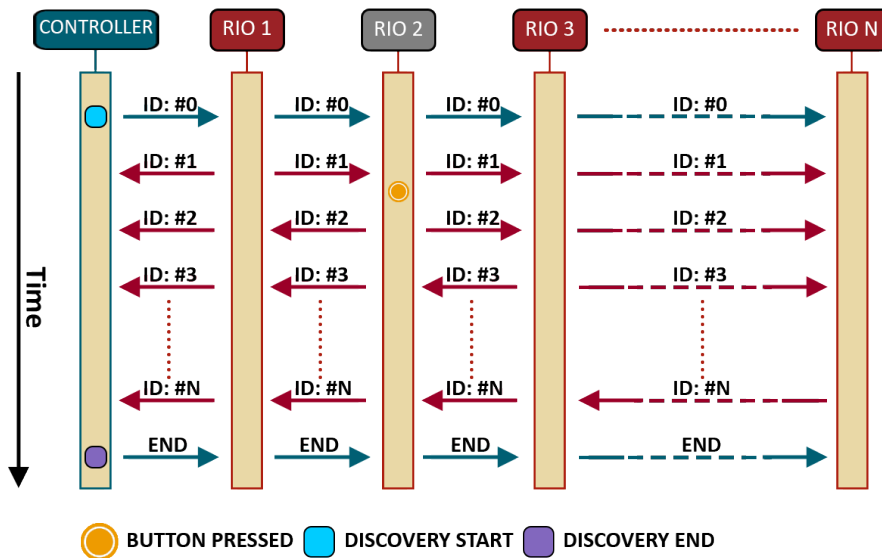
Figure 3.14: Diagram of the discovery procedure executed at the first startup.

To light the smart tiles as the game logic demand, the controller board must know their relative spatial position. The first requirement is to know the floor geometry to program the game logic consequently; our smart floor is a rectangle 4 meters large and 2 meters long. Secondary, each tile must have an identification number or ID. Through a direct correspondence between a position and an ID, the controller can light the tiles correctly. The discovery phase allows making this connection. Each

RIO board has a user button, pressing it during such a routine allows the memori-sation of the ID inside the RIO memory. The sequence with which the buttons are pressed changes the IDs linked to the positions, thus changing the behaviour of the system.

Figure 3.14 explains the discovery phase through a diagram. Each RIO board does not have an ID assigned and saved inside its memory at the first startup. Initially, the controller board broadcast a discovery start message over the I^2C bus to tell the boards that the procedure is starting; such message contains the value 0. In Figure 3.14 the first line of arrows represents the discovery start message. Nothing happens until the pressure of a RIO's button; then, the selected board saven the value one in-side of its memory and broadcasts it over the bus. Such transmission is represented by the first line of red arrows in Figure 3.14. The same behaviour happens for the suc-cessive boards, each time increasing by one the value transmitted until the number of RIOs which control the floor is reached. Finally, the controller board broadcast an end message to end the discovery phase (the bottom line of blue arrows in Figure 3.14). No button needs to be pressed at the next startups of the smart floor. Indeed, knowing their IDs, the RIO boards transmit it over the bus after the reception of their previous one.

In the case of a RIO board substitution, the discovery phase can end anyway, even if the new board does not have an ID assigned. The only action necessary to complete the communication is to press the button on the new board. Indeed, the transmission goes on until the substituted board must transmit its ID over the bus. Unable to send its ID, the new RIO waits for its button's pressure, while the successive boards wait to receive their previous ID. When the button is pressed, the communications resume and the discovery phase can end.

The calibration phase

After the end of the discovery phase, the controller board sends a broadcast message of calibration start. The RIO boards polarise the conditioning circuits by changing the DAC outputs. When the board with ID one has completed the calibration, it sends a broadcast message of calibration terminated over the I^2C bus. After finishing their

calibration, the other boards wait for the message from their previous one before sending their own, as it happens for the discovery phase. The calibration can provide three possible outputs:

- Calibration_ok: when all the conditioning circuits have been polarised correctly.

- Calibration_partially_ok: when one sensor of a tile is not working.

- Calibration_error: when more than one tile sensor does not work.

If just one tile provides a Calibration_error message, the smart floor cannot start any game. Instead, the smart floor can start the games in the presence of multiple Calibration_partially_ok messages. This last eventuality reduces the sensing capability of the system. If the calibration is successful (or partially successful), the system connects to the server. The successive messages that run over the I^{2}C bus are commands and information that the controller and the RIOs exchange, respectively.

The calibration algorithm

The calibration algorithm aims to have each output close to the bottom knee of its characteristic; referring to equation 3.4, it searches for the values closest to:

$$V_{DAC,i} = V_{Y,i}; \ V_{OUT,i} = 0$$

where i goes from 1 to 8 and represents the different channels.

The DAC starts the calibration by outputting 1.65 volts on each channel. Successively, the ADC sample the output values of the conditioning circuits. Consider the case of a single channel; if the sample falls in the saturation zones or the top part of the gain stage, the DAC output change with the bisection method. Instead, if the sample falls in the bottom part of the gain stage, the DAC output changes by unitary steps for fine-tuning. When the samples are relatively close to zero, the calibration for that circuit is completed. Figure 3.15 shows the steps of the calibration for one conditioning circuit. The first three steps fall in the saturation zones, and the successive ones move towards the bottom knee. The sixth step falls in the bottom part of the gain stage; the value changes unitary after that.
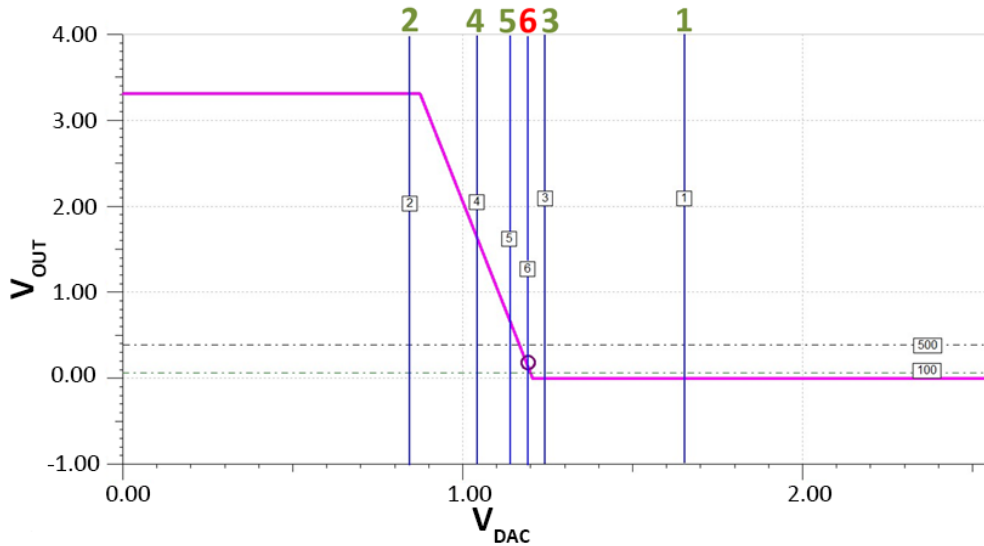
Figure 3.15: Steps of the calibration procedure.

3.2.5 Wi-Fi communications

After the discovery and calibration phases, the controller board starts the connection to an access point. Then, it creates an encrypted connection to the server. The connection uses the TCP (Transmission Control Protocol) and the TLS (Transport Layer Security) protocols to have a reliable communication channel. Over the encrypted channel runs an MQTT[7] service; at this point, each message exchanged between the smart floor and the server is an MQTT message which passes over a dedicated MQTT topic. At this point, the system waits for a user command. The user can interact with the smart floor through a dedicated web app that shows the performances at the game end. The web app allows running different games at different difficulty levels.

The MQTT messages

When the user selects a game and its difficulty, the web app sends an MQTT message to the broker, which shares it with the smart floor. The administrator of the system

---

[7]https://mqtt.org/

Table 3.1: The JSON strings that control the smart floor.

Command	Description
{'cmd':'dac_calibrate'}	The device performs a new calibration.
{'cmd':'game_start_ <game_id> _<difficulty>_<match_id>'}	The game with id <game_id>starts, with a difficulty chosen by the parameter <difficulty>.

Table 3.2: The JSON fields used to transmit the elaborated data.

Field	Type	Description
measure	string	Measure name
measure_unit	string	Measure unit
data_type	string	Measure description
data_source	string	The object which has generated the measure
values	JSON array	The measure values

has an additional command which allows performing a new calibration of the sensors. The MQTT messages are in JSON[8] (JavaScript Object Notation) format, and Table 3.1 shows their syntax. After the game ends, the controller board elaborates all the data gathered and provides the results to the server. Even the results are transmitted in JSON format. Table 3.2 shows the structure of the results; such a scheme can contain all the metrics necessary for the specific game in execution.

The structure of the messages and the MQTT service allows running multiple smart floors and other smart objects simultaneously. Indeed, changing the MQTT topic on which each smart floor communicates allows routing the communications at the correct receiver.

---

[8]https://www.json.org/json-it.html

3.2.6   The design of the games
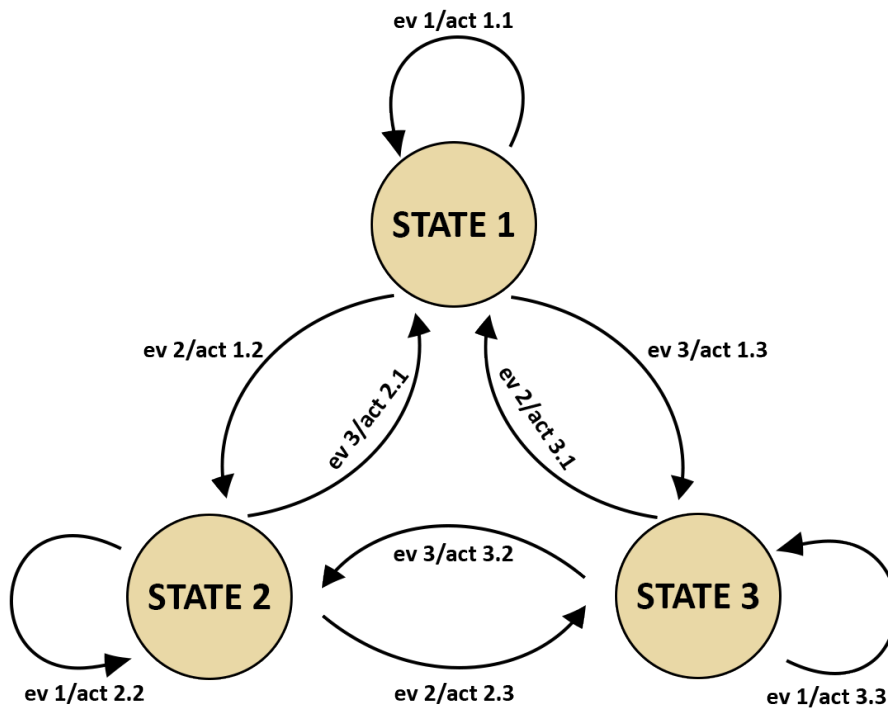
Figure 3.16: The structure of the states machine.

Every game designed for the smart floor system or the other objects (smart table and smart bench), was initially described as a Mealy state machine. This representation allowed for a readable structure and minimised possible errors and missed transitions. The number of states not considered in the algorithm, thus a possible game block, was drastically reduced through such a methodology. Adopting this description and considering the inputs and outputs of the smart floor allows for a diversity of behaviours.

Figure 3.16 shows an example of a Mealy machine with three states. The arrows represent the rising of an event and its relative action; they connect the states be-

tween them or with themself. In Figure 3.16, the events and the actions are named respectively, *ev x* and *act y.z*, where *x* is the number of the event, *y* is the number of the starting state, and *z* is the number of the ending state. Each event can start from any state; however, the relative action can change depending on the starting and ending states. Each state in Figure 3.16 has three events, but a given state can have fewer events. The behaviour desired for the smart floor determines the transitions, the events, the actions and their number.

The state machine for the "Molten floor" game

Table 3.3: The table of transitions for the molten floor game.

	IDLE	READY	WAITING_FOR_DATA
nil_event	IDLE;	READY;	WAITING_FOR_DATA;
	nil_action	nil_action	waiting_for_data_timeout_check
mqtt_game_start	READY;	READY;	WAITING_FOR_DATA;
	idle_to_ready	nil_action	nil_action
start_tile_pressed	IDLE;	WAITING_FOR_DATA;	WAITING_FOR_DATA;
	nil_action	ready_to_data_waiting	nil_action
new_data_arrived	IDLE;	READY;	WAITING_FOR_DATA;
	nil_action	nil_action	on_data_arrival_action
path_cleared	IDLE;	READY;	IDLE;
	nil_action	nil_action	path_cleared_action
inactivity_timeout	IDLE;	READY;	IDLE;
	nil_action	nil_action	path_cleared_action
game_timeout	IDLE;	READY;	IDLE;
	nil_action	nil_action	path_cleared_action

The molten floor game was designed through a state machine; the game use only three states but seven possible events. The game's goal is to jump over all the green tiles while avoiding touching the others; in the shortest time possible. Table 3.3 shows the table of transitions for the molten floor game, which is the reproduction of the

state machine in a tabular form. Inside this table is described how the system responds to an event for each state. The syntax inside the cells is $NEXT\_STATE$; *action*, where $NEXT\_STATE$ is the successive state and *action* is the action to do. The three possible states are:

- **IDLE**: where the system is waiting for a start game command.

- **READY**: where the system is waiting for the pressure of the initial tile.

- **WAITING_FOR_DATA**: where the game is started, and the system is waiting for events to happen.

Is possible to switch between the states through the seven possible events, which are:

- **nil_event**: when nothing happens.

- **mqtt_game_start**: when a start game message arrives.

- **start_tile_pressed**: when the first tile of the path is pressed.

- **new_data_arrived**: when a tile changes its state.

- **path_cleared**: when the game is completed.

- **inactivity_timeout**: when no action happens on the floor for a specific time.

- **game_timeout**: when the maximum time allowed to complete the game is expired.

The combination of events and states brought six different possible actions. Such actions are the response of the system to a specific interaction. The actions are:

- **nil_action**: nothing happens.

- **idle_to_ready**: the controller generates the path and lights up the initial tile with green.

- **ready_to_data_waiting**: all the tiles blink in green; then every light is switched off, and successively the path lights up in green.

- **waiting_for_data_timeout_check**: the controller checks if the timeouts are expired.

- **on_data_arrival_action**: the controller manages the tile's state transition, lights up the LED strip with the proper colour and checks if the game is completed.

- **path_cleared_action**: the controller elaborates the data and sends them to the server with an MQTT publish; then, it brings the smart floor to the IDLE state waiting for a command.

Chapter 4

Evaluation of the systems

Here are presented and examined the results of the systems described in Chapters 2 and 3. Regarding the BCG/SCG system, the following pages describe the databases we recorded with the acquisition systems. Together with the results, even the metrics for evaluating the heartbeats identification algorithm are presented and discussed. Instead, the smart floor system evaluation focused on two different aspects. The first is the engagement of the user and the stimulus that the device brings in repeating the experience. The second one is more technical and involves the system's ability to sense little pressures and the correct electrical response by the conditioning circuit.

4.1   The BCG and SCG system

We tested the algorithm's ability to identify heartbeats by analysing different BCG and SCG databases that we recorded. It is important to remember that we acquired the databases at different times and that the methodologies and the devices evolved after each experience.

The same results presented in this section have already been published in [68].

4.1.1   Changes in waveforms versus ideality

Many factors can corrupt a BCG or SCG waveform by introducing undesired arte-facts inside the signals. Sometimes, the corruption can be too strong to cover one or multiple heartbeats completely; thus, identification can be almost impossible. For example, one source of the problem can be the subject's movements during the ac-quisition of the signals.

Other types of corruption can be less disruptive, and even if they introduce changes inside the measures, the caused distortion is not too worrying. Often, such distortion is not avoidable because it involves aspects of the measures that cannot be changed easily. For example, for BCG, the type of bed, its mechanical structure, and the posi-tion of the accelerometer change the sensing device's mechanical coupling with the subject's body. Even how we sleep (prone, supine, etc.) influences the resulting sig-nals. For SCG, the waveform change with the position of the accelerometer over the body. Moreover, the body structure itself changes the morphology of the waveforms, both for SCG and BCG.

Many of these influences cannot be removed easily from the signals; thus, the algo-rithm that analyses the waveforms should be robust enough to overcome and possibly identify them.

The morphology changes can manifest as additional peaks or valleys or changes in the main peaks' magnitude. When large body movements are involved, the wave-forms can become wholly unrecognisable and contain high variations.

For the databases we acquired, the subjects were instructed to stand still and make little body movements if necessary; thus, our recordings do not contain important movement variations. Such lack is both an advantage and a limitation, indeed with clean waveforms is possible to verify the algorithm's behaviour in the desired condi-tions, but it is impossible to test its robustness when spikes come.

4.1.2   The experimental setups and the databases

We have acquired three different datasets: two involve BCG traces, whereas the re-maining contains SCG curves. To record them, we used the acquisition systems de-

signed; in particular, datasets SCG-1 and BCG-1 used an ARM Cortex M0+ configuration (the Arduino board); instead, dataset BCG-2 used an ARM Cortex M4 configuration (the B-L475E-IOT01A board). We have recorded a synchronous ECG in all the databases as a reference for evaluating the heartbeat identification methodology. All the subjects involved were healthy volunteers without any known heart diseases; the studies were conducted following Helsinki's declaration on ethical principles. The analysis also involved an external database publicly available.

Table 4.1 summarises the datasets; ID is the name of the dataset, N_{rec} is the number of records in the dataset, F_s is the sampling frequency, and the field Provenance tells if the database was acquired by us or obtained online.

Table 4.1: List of the databases analysed.

ID	N_{rec}	F_s	Description	Provenance
SCG-1	13	100 Hz	SCG database of sitting subjects	Acquired
SCG-2	20	500 Hz	CEBS database: SCG of lying subjects	Online
BCG-1	18	250 Hz	BCG database: bed frame 1	Acquired
BCG-2	42	500 Hz	BCG database: bed frame 2, three lying position for each subject	Acquired

The SCG-1 database

Dataset SCG-1 contains the signals of 13 volunteers acquired while subjects were comfortably sitting on a chair in an upright position. Nine males and four women participated in the study (age 35.2 ± 16.0); each recording lasted 4 minutes.

We inserted the accelerometer used for the measures inside a plastic container to achieve electrical isolation, successively we placed it over the subjects' sternum. Moreover, a chest strap has held the sensor in place to attain good signal quality. We acquired a lead-I ECG simultaneously through disposable Ag/AgCl electrodes placed on the subjects' left and right shoulders. To reduce common-mode noise, we added a DRL electrode attached to the right hip.
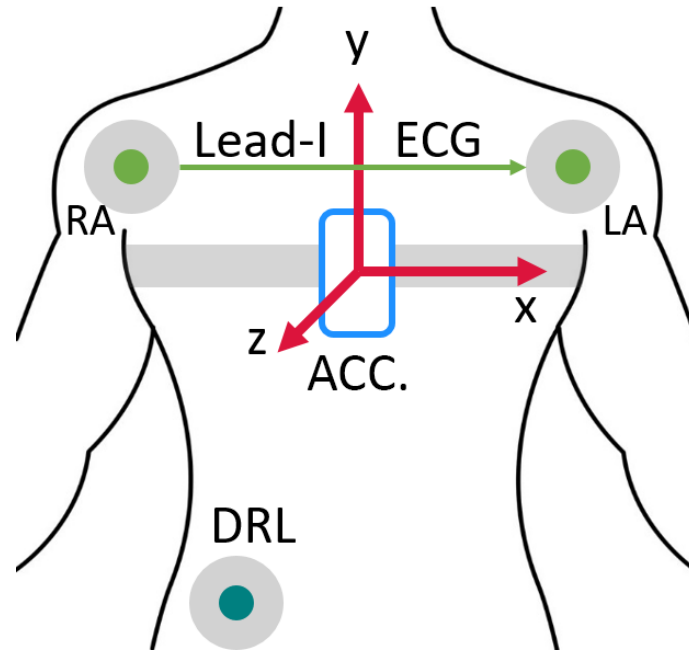
Figure 4.1: The placement of the accelerometer and the electrodes over the body of the subject. The ECG is acquired through the right arm and left arm electrodes, respectively named RA and LA, whereas DRL means Driven Right Leg and is the electrode used to reduce the measure's common-mode interference.

The MCU samples with a frequency of 100 Hz as a compromise between low power consumption and time resolution, looking forward to an embedded device. Figure 4.1 shows the accelerometer placement and its orientation respectively to the body, together with the placement of ECG electrodes. The same setup and database are studied also in [45, 116, 117].

The SCG-2 or CEBS database

SCG-2 is the CEBS database (Combined measurement of ECG, Breathing and Seismocardiogram) [124, 125], a public dataset hosted on PhysioNet [126]. It contains the

signals recorded from 20 healthy subjects lying supine on a bed. SCG signal, lead-I and II ECG derivations and breath signals were simultaneously sampled through a Biopac MP36 data acquisition system (Santa Barbara, CA, USA). In particular, a tri-axial accelerometer produced the SCG signals, though, because the dorso-ventral axis expresses the most relevant information, this direction is the only one available. The length of a single record is around 50 minutes each, for a total of about 69,500 heartbeats. Such a length allows validating the methodologies in time intervals relatively significant. In [124, 125, 126] are described more details on the methods and the database. We proposed a methodology to analyse SCG-2 in [116] and we have deepened the analysis in [51] through a convolutional variational autoencoder network.

The main differences between the SCG databases' setups are the subject's position (sitting for SCG-1 and lying for SCG-2) and the sampling frequency (100 Hz for SCG-1, and 5000 Hz for SCG-2, downsampled to 500 Hz for easier processing).

The BCG-1 database
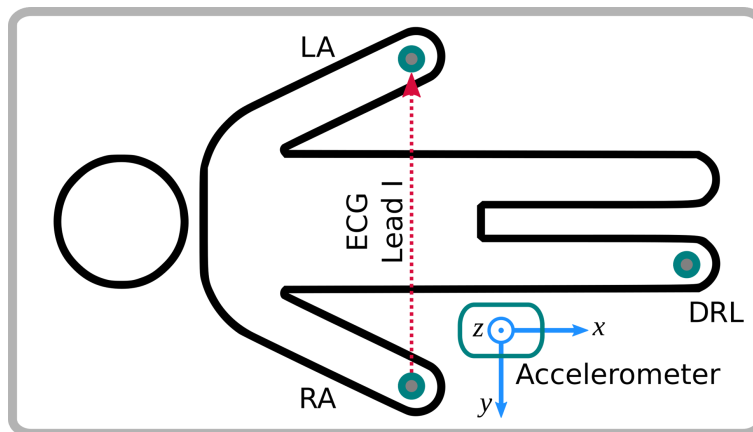
Figure 4.2: The top view of the subject lying on the bed with the electrodes, the accelerometer and its orientation system visible.

The third dataset, BCG-1, collects 18 recordings lasting 5 minutes each, obtained

from healthy volunteers. As Figure 4.2 shows, the subjects were lying supine on a rigid frame bed during BCG and ECG concurrent measurements. The same acquisition system used for the SCG-1 database sensed the signals. Different from SCG-1, we used a sampling frequency of 250 Hz. Figure 4.2 also illustrates the placement of the device; the three electrodes were placed on the left arm, the right arm, and the right leg (LA, RA and DRL, respectively); the last electrode is used to reduce the common-mode interferences. Instead, the accelerometer was firmly placed upon the bed, on the subjects' right. The same setup and database are also studied in [118].

The BCG-2 database
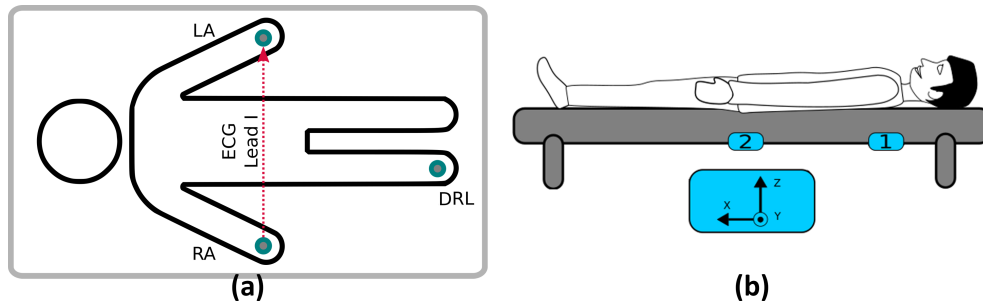
Figure 4.3: **(a)** The top view of the subject lying on the bed; the positions of the electrodes are visible. **(b)** The side view of the subject lying on the bed; the position of the accelerometers and their reference system are highlighted.

The last database, BCG-2, contains the signals recorded from 14 healthy volunteers; each subject was asked to lie in three positions; we have acquired 42 records thus. The participants were 13 males and one female, with an average age of 27.1 years. Due to the COVID-19 pandemic, obtaining a more balanced (males/females) and large database was impossible. The same setup and database are also studied in [119].

We followed a precise measurement protocol to record the signals; each subject was instructed about the protocol before starting the measures. The measurement protocol is the following:

- The subject lies down supine; the signals are recorded for five minutes.

- After a one-minute break, the subject moves to a left-side position; again, we recorded the signals for five minutes.

- After another one-minute break, the subject moves to a right-side position; we acquired the last five minutes of data.

Unlike the other datasets, the MCU that controls the acquisition was an ARM Cortex M4. Other changes involved the sampling frequency, which was set to 500 Hz and the bed, which had a spring frame. Moreover, the acquisition system employed two synchronous ADXL355 accelerometers. The devices were firmly attached under the bed frame through tape. As Figure 4.2b shows, we placed accelerometer one under the subject's chest, and accelerometer two was approximately under the subject's centre of mass. The figure also shows the reference system of the accelerometers:

- The x-axis represents the head-to-foot component.

- The y-axis represents the lateral component.

- The z-axis represents the dorso-ventral component.

Figure 4.2a shows the ECG electrodes placement used to acquire a lead-I derivation. Instead, Table 4.2 reports other statistics about the subjects under test.

Table 4.2: Statistical data of age, weight and Body Mass Index (BMI) for the subjects of database BCG-2.

Age	Weight [kg]	BMI [kg/m^2]
27.07 ±6.31	77.71 ±11.73	24.46 ±3.22

4.1.3 Evaluation metrics

To better understand the algorithm abilities of heartbeats identification and compare them with others present in the literature, it is helpful to obtain some evaluation metrics. The algorithm's abilities evaluated are:

1. Its heartbeats detection abilities.

2. Its ability of heartbeats precise time localisation.

We can evaluate such properties by comparing the ECG's reference points (the gold standard) and our algorithm's outputs. Such comparison is possible thanks to the assumption of a regular heartbeat; in fact, the absence of rhythm disturbances makes it possible to correlate the mechanical and electrical activities of the heart. For ECG, the R-peaks inside the QRS complexes are used as heartbeat references; such points were obtained through the Pan-Tompkins algorithm [33] and a manual check. Instead, how our algorithm produces its outputs is discussed in Section 2.2.2.
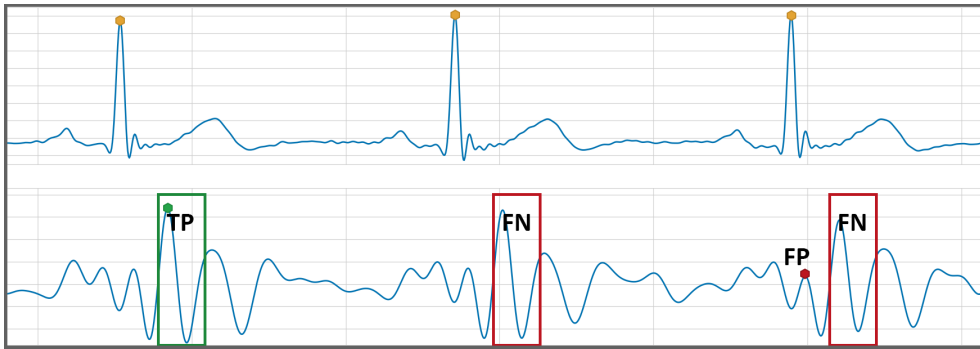
Figure 4.4: A graphical explanation of TP, FP, and FN conditions. The squares represent the different tolerance windows, the yellow marks are the R-peaks and the green and red marks are the reference points.

To understand how the evaluation of the output is made is helpful to introduce some definitions first. In the following, I will refer to the heartbeats position identified by our algorithm with the words reference points.
For each R-peak is defined a 100 ms tolerance window where the respective reference point should be found. The time position of the windows is subject-dependent and can be obtained by statistical esteem of the distance between the prototype (more information about the prototype in Section 2.2.2) and the R-peaks positions. It is important to remember that such statistical measure is used only for performance assessment

purposes. With such a premise, the following definitions (graphically visible in Figure 4.4) explain how the evaluation algorithm can mark the reference points:

- A reference point is considered correctly detected and labeled as **True Positive (TP)** if its position falls within the tolerance window.

- If a reference point is identified outside of its tolerance window, it is considered a **False Positive (FP)**.

- If a tolerance window does not contain any reference point, it is considered a **False Negative (FN)**.

With such definitions is possible to introduce the following metrics:

- **Sensitivity**: the percentage of reference points correctly identified.

$$Sens. = \frac{TP}{TP+FN} \tag{4.1}$$

- **Precision**: the percentage of right detection among all the detection.

$$Prec. = \frac{TP}{TP+FP} \tag{4.2}$$

The correctly detected beats can be used to verify the ability of precise heartbeats localization in time. It is helpful to define the R-R intervals' time series and the time series of the complex-to-complex intervals:

$$t_{RR} = \{t_{R,i} - t_{R,i-1}\}, i \in \{1, ..., N-1\} \tag{4.3}$$

$$t_{CC} = \{t_{C,i} - t_{C,i-1}\}, i \in \{1, ..., N-1\} \tag{4.4}$$

Where N is the number of correctly detected heartbeats. Using equations 4.3 and 4.4 the annotation error can be defined as:

$$e_i = t_{RR,i} - t_{CC,i} \tag{4.5}$$

With equation 4.5 is possible to define the following metrics of evaluation:

- **Root Mean Square Error (RMSE)**

$$RMSE = \sqrt{\frac{1}{N-1} \cdot \sum_{i=1}^{N-1} e_i^2} \qquad (4.6)$$

- **Mean Absolute Error (MAE)**

$$MAE = \frac{1}{N-1} \cdot \sum_{i=1}^{N-1} |e_i| \qquad (4.7)$$

The two metrics reveal the discrepancy between the reference points and the R-peaks positions. Even if RMSE and MAE are similar, it is important to provide both because they can be helpful for different purposes. Indeed, the first one gives more weight to large errors than the second; this implies that it is better to consider one or the other depending on how important the errors are.

The definitions previously listed are valid for the analysis of both BCG and SCG because, even if the nature of the signals is different, the information they provide is similar.

4.1.4   Experimental results

Before presenting and discussing the results is worth noting that to keep the results consistent between the databases, we analysed only a portion of the signals acquired, in particular:

- The results of database SCG-1 come from the analysis of the axis perpendicular to the chest (the z-axis of Figure 4.1). Such a choice allows a correct comparison with database SCG-2.

- Because the recoil forces that produce the BCG are mainly in the head-to-foot direction [77], the results of both BCG databases come from the analysis of such a component (the x-axis of Figure 4.2 and Figure 4.3b).

- Even if the acquisition system of BCG-2 featured two accelerometers (see Figure 4.3b as reference), we analysed only number one. Indeed, accelerometer

two was introduced in the system for future studies. Its signals are not used in the present analysis because they do not provide additional information on the algorithm's qualities.

Table 4.3: The average score and 10th Lowest Performance Percentile (LPP) for each metric and dataset.

	Sensitivity [%]	Precision [%]	RMSE [ms]	MAE [ms]
SCG-1				
mean	98.9	97.9	8.1	4.8
10th LPP	96.2	96.3	8.2	5.7
SCG-2				
mean	98.5	98.6	4.5	3.3
10th LPP	97.0	97.2	6.1	4.8
BCG-1				
mean	98.4	97.6	6.8	5.0
10th LPP	96.7	95.0	10.6	7.9
BCG-2				
mean	98.2	98.0	5.6	3.6
10th LPP	96.2	96.4	8.8	5.9

We obtained the metrics described in Section 4.1.3 from all available datasets. Table 4.3 reports such results for each metric in terms of average and 10th Lowest Performance Percentile (LPP). In the following paragraphs, the scores are always listed in the order SCG-1, SCG-2, BCG-1 and BCG-2.

As stated before, the results presented in this section were already published in [68] by the same author. However, other publications analysed BCG databases [118, 119] and SCG databases [45, 51, 116, 117] through a similar algorithm. Such works come from the same author of this thesis, and often present the scores on the singular records.

Sensitivity and precision are the metrics to consider to assess the most crucial
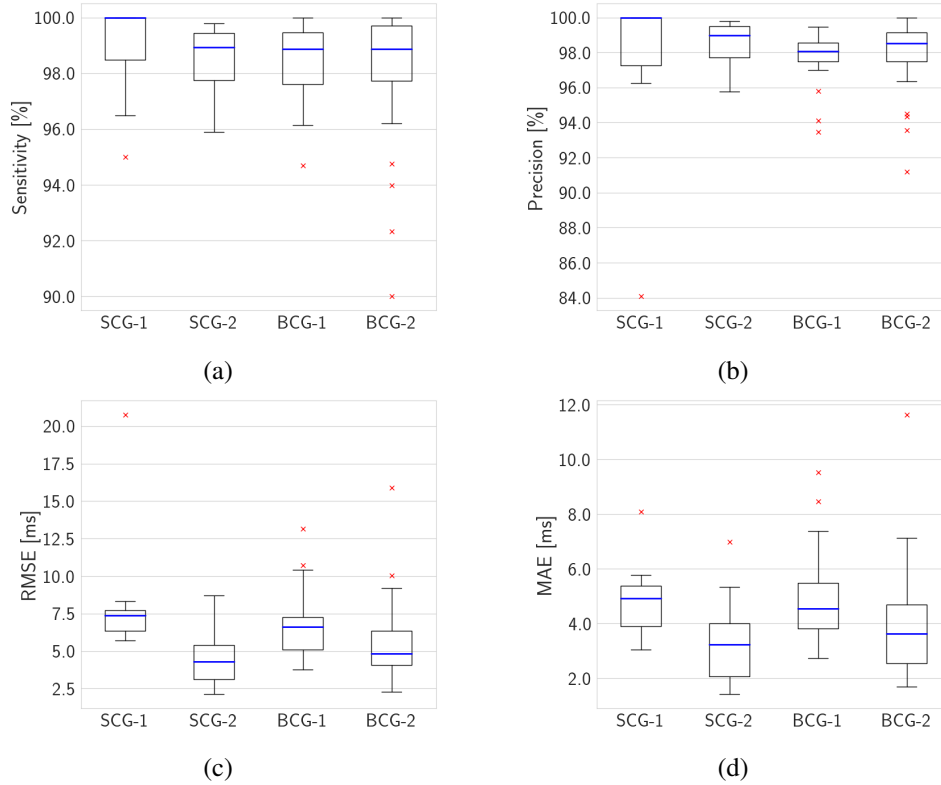
Figure 4.5: The Box-plots of: **(a)** Sensitivity, **(b)** Precision, **(c)** RMSE, **(d)** MAE.

quality of the algorithm, the ability of heartbeats detection. On average, sensitivity obtained the values 98.9%, 98.5%, 98.4% and 98.2% whereas the 10th LPP scored 96.2%, 97.0%, 96.7% and 96.2%. Such results prove that the majority of heartbeats can be detected. Taking into account precision scores, their average values are 97.9%, 98.6%, 97.6% and 98.0%, with 10th LPP values of 96.3%, 97.2%, 95.0% and 96.4%. Even for precision, the performances are high, meaning that the algorithm has a low rate of false positives creation. Furthermore, as LPP values show, both metrics remain stable at high values even considering the entire population. Figures 4.5a and 4.5b give a graphical representation of the distribution of the scores for sensitivity and precision, respectively. Together, the scores of sensitivity and precision confirm that

the methodology adopted can be a good resource to detect heartbeats inside SCG and BCG signals without using the ECG.

RMSE and MAE are the metrics used to evaluate the ability of precise temporal localisation of heartbeats. Figures 4.5c and 4.5d show the distribution of RMSE and MAE performance, respectively. The average values obtained by RMSE are 8.1, 4.5, 6.8 and 5.6 ms, and the 10th LPP are 8.2, 6.1, 10.6 and 8.8 ms. Instead, the average MAE's scores are 4.8, 3.3, 5.0 and 3.6 ms, with 5.7, 4.8, 7.9 and 5.9 ms as 10th LPP. As the scores tell, the methodology adopted can provide precise temporal localisation with errors of a few ms. A representation valuable for comprehending
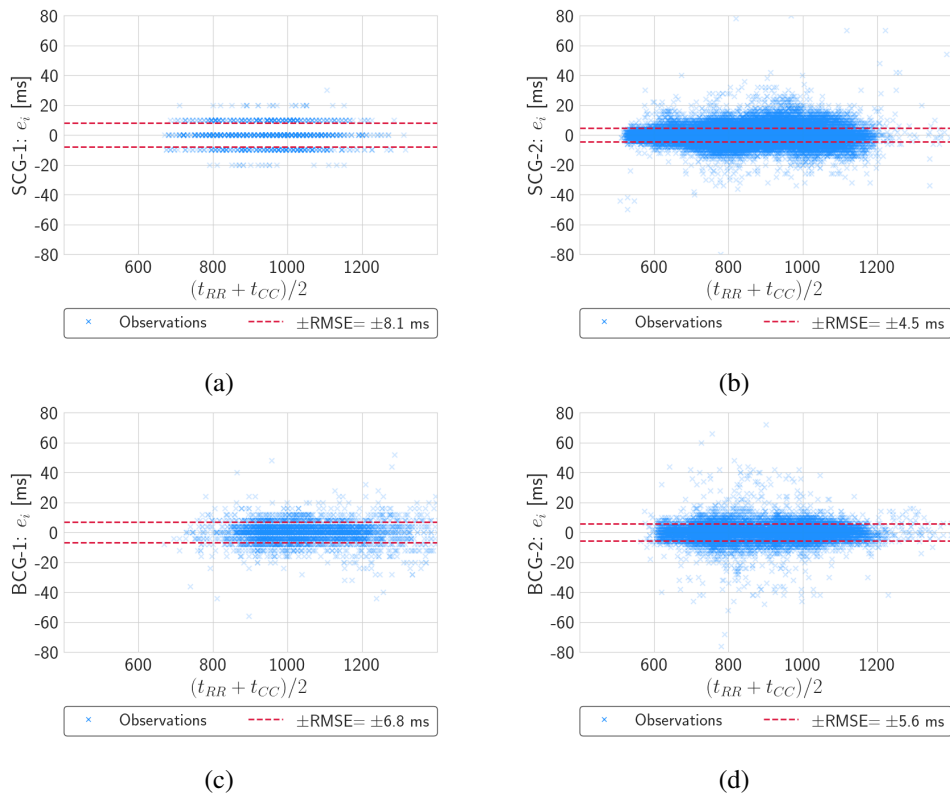
Figure 4.6: Bland-Altman plots of the t_{RR}, t_{CC} closeness; **(a)** SCG-1, **(b)** SCG-2, **(c)** BCG-1, **(d)** BCG-2.

the temporal localisation of our methodology is shown in Figure 4.6, which displays Bland–Altman plots for all four datasets. Such plots represent the closeness of the t_{RR} and t_{CC} intervals values. On these graphs, the x-axis contains the average of the intervals, in mathematical language: $(t_{RR,i} + t_{CC,i})/2$, whereas the y-axis contains the measurements errors e_i. By examining such plots, it is possible to see that errors are distributed relatively evenly around zero, another confirmation of the correctness of the methodology.
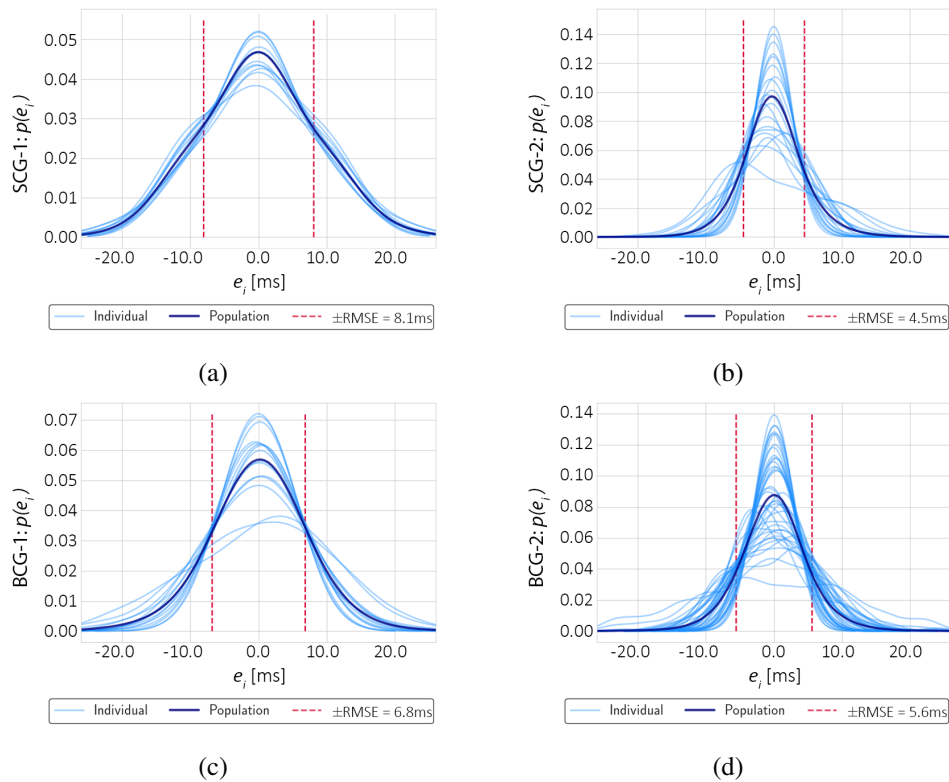
Figure 4.7: Kernel Density Estimates (KDE) of e_i for datasets: **(a)** SCG-1, **(b)** SCG-2, **(c)** BCG-1, **(d)** BCG-2.

With Bland-Altmann plots is possible to identify dependencies between intervals and measures graphically. For example, Figure 4.6a shows a separation between

the points in distinct lines for dataset SCG-1; such separation is due to the limited sampling frequency used, which does not allow a finer temporal resolution. Similar, but softer, behaviour is shown in Figure 4.6c for dataset BCG-1. This dependence reflects on MAE and RMSE results; indeed, datasets with lower F_s shows higher values caused by a less fine temporal resolution.

Another way to comprehend the agreement between the beat-to-beat intervals provided by our algorithm and the ECG is through the graphs of Figure 4.8, which are Kernel Density Estimation (KDE) of the errors e_i. KDE is a methodology that provides a Probability Density Function (PDF) starting from data points. To produce the graphs, we used a Gaussian kernel with a bandwidth parameter set to one sampling interval $T_s = 1/F_s$. In the graphs of Figure 4.8, the light blue traces are the KDE for each subject; the tick dark blue line represents the population-wide aggregation; the red dotted lines represent the ±RMSE values. As visible from the KDE plots, the errors e_i show a zero-mean distribution for each dataset; instead, they tend to be less concentrated depending on the sampling period. Indeed, the 95% Highest Density Interval (HDI), where the 95% of points fall, is $\approx$ 20 ms for SCG-1 (Ts = 10 ms, Figure 4.7a), $\approx$ 16 ms for BCG-1 (Ts = 4 ms, Figure 4.7c), $\approx$ 10 ms for SCG-2 and BCG-2 (Ts = 2 ms, Figure 4.7b and 4.7d, respectively).

(a) (b) (c)
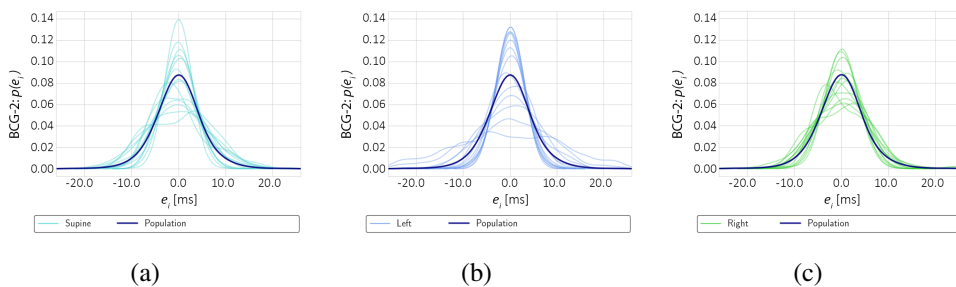
Figure 4.8: Kernel Density Estimates (KDE) of e_i for dataset BCG-2, grouped by lying position.

The charts in Figure 4.8 show KDE for the database BCG-2 grouped by resting position; supine, left position, and right position for Figures 4.8a, 4.8b, 4.8c, respectively. The precedent discussion is also valid for those graphs, which provide similar

results. No significant differences are visible between the KDE, which suggests no differences in the algorithm's performances due to the position. A more rigorous proof of such a characteristic is discussed in the following paragraphs.

4.1.5 Discussion of results

We assessed the proposed methodology on four different datasets, which differ by the time of measure, aim, temporal resolution and measurement protocol. Therefore, we explored a wide range of scenarios. To identify possible differences in the algorithm behaviour between different datasets, we used two statistical tests:

- the Kruskal–Wallis test is a non-parametric test that asses if the results come from the same distribution or not. Such a test allows verifying if the methodology behaves differently between different datasets.

- the Mann–Whitney U test is similar to Kruskal–Wallis but analyse only two populations.

Because to use such tests we performed multiple comparisons, we adjusted the p-values through the Benjamini–Hochberg correction: $p_{adj} = p \cdot M/r_i$, where M is the number of tests conducted, and r_i is the rank of the i-th p-value in ascending order. The following paragraphs present the results of the tests; in the tables that summarise the results, we use the following notation: a single asterisk indicates significance at the 0.05 level; a double asterisk indicates significance at the 0.01 level.

Table 4.4: Results of the Kruskal–Wallis test for differences between lying positions in dataset BCG-2.

	p_{adj}	$p_{adj} < 0.05$	$p_{adj} < 0.01$
Sensitivity	0.9057		
Precision	0.9677		
RMSE	0.7842		
MAE	0.5213		

Initially, we tested the difference in results between the lying positions of dataset BCG-2 to verify if there was an influence on the performances. The results reported in Table 4.4 show that the hypothesis of belonging to the same distribution cannot be rejected for all the metrics. Thus, we can consider the results of BCG-2 together when discussing performances because the position does not influence the methodology.

Table 4.5: Results of the Kruskal–Wallis test for differences between datasets.

	p_{adj}	$p_{adj} < 0.05$	$p_{adj} < 0.01$
Sensitivity	0.6290		
Precision	0.0663		
RMSE	0.0003	*	**
MAE	0.0036	*	**

Table 4.5 shows the results of the Kruskal–Wallis test, which searches for differences between all datasets' performance. Statistically, sensitivity and precision cannot reject the null hypothesis of belonging to the same distribution; instead, RMSE and MAE reject it ($p_{adj} < 0.01$). The first results imply that the detection of heartbeats is consistent between different datasets. Instead, the RMSE and MAE results need further exploration to understand why different datasets provide different results.

As mentioned, Mann-Whitney tests were performed to unravel the differences between couples of datasets. Table 4.6 presents the results of such an investigation on RMSE and MAE values; differences emerge in the scores:

- SCG-1 results are significantly different from SCG-2 and BCG-2 ones. As discussed in the previous section, the limited sampling interval of SCG-1 ($T_s = 10$ ms) impacts the performances. Indeed, fine temporal annotation strongly depends on temporal resolution. Such conclusions are supported by the differences between RMSE and MAE average values reported in Table 4.3.

- BCG-1 scores behave similarly to the SCG-1 ones, even if the differences with the other two datasets are less hard.

Table 4.6: The results of the Mann-Whitney tests used to identify differences between datasets.

Metric	Dataset a	Dataset b	p_{adj}	$p_{adj} < 0.05$	$p_{adj} < 0.01$
RMSE	SCG-1	SCG-2	0.0006	*	**
	SCG-1	BCG-1	0.1422		
	SCG-1	BCG-2	0.0083	*	**
	SCG-2	BCG-1	0.0117	*	
	SCG-2	BCG-2	0.0686		
	BCG-1	BCG-2	0.0502		
MAE	SCG-1	SCG-2	0.0121	*	
	SCG-1	BCG-1	0.4762		
	SCG-1	BCG-2	0.0273	*	
	SCG-2	BCG-1	0.0117	*	
	SCG-2	BCG-2	0.1501		
	BCG-1	BCG-2	0.0331	*	

• Datasets SCG-2 and BCG-2 do not show any statistical difference.

The results suggest that the sampling frequency F_s should be increased to have a finer annotation and beat-to-beat intervals more precise. However, increasing the sampling frequency can be difficult in some scenarios, such as when power saving is crucial.

4.2 The smart floor system
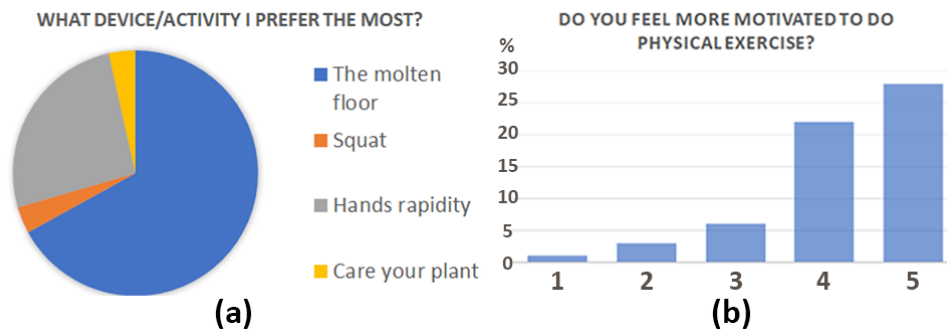
Figure 4.9: **(a)** The appreciation of the molten floor game. **(b)** The stimulus of active behaviour.

The PLEINAIR project was presented to the public on 27th October 2021 at the museum of peasant civilisation in Bentivoglio, an Italian municipality in the Emilia Romagna region. The smart floor and other smart objects were some of its attractions. During the event, sixty people tested the floor and the other objects designed. The users were asked to take a survey, which was made to analyse their impressions in terms of engagement and stimulation in active behaviour. Figure 4.9a shows the appreciation of the smart floor and the molten floor game by the users. Instead, Figure 4.9b reports the answers to the question: "Do you feel more motivated to do physical exercise?". The results show that almost 47% of the users felt more motivated.

Such preliminary data suggest that the objects designed (the smart floor in particular) can be instruments adequate to stimulate healthier behaviours.

4.2.1 Experimental results

To match the requirement of little weights detection, we tested the smart tile with a series of experimental measures. After having built and polarised the device as described in the previous chapters, we used an oscilloscope and a multimeter to measure the system's response to an applied mass. We applied the mass through sand and

a plastic container. The sand was added gradually and always previously weighted through a weighing scale. The measures were taken starting from 0 kilograms to 2 kilograms and repeated for different zones of the tile.

The conditioning circuit response and the resistance variation
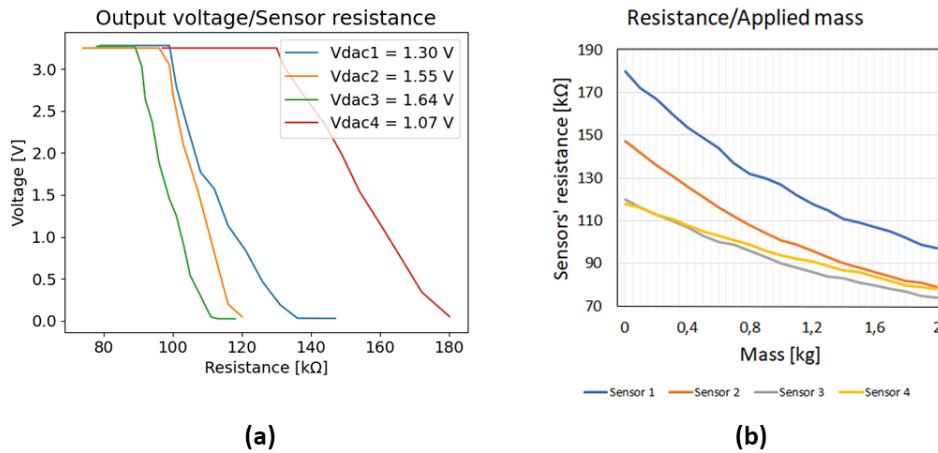
Figure 4.10: **(a)** Input-output characteristic of one conditioning circuit, obtained through the measures. **(b)** Resistance variation due to an applied mass.

Initially, we assessed the correct behaviour of the conditioning circuits and the sensors through dedicated measures. Figures 4.10a and b show the results of such measures for four conditioning circuits and sensors. The measurements were obtained by incrementally applying a mass over the tile with steps of 100 grams; the mass was placed over the various sensors' positions. Figure 4.10a shows the input-output characteristic of the conditioning circuit obtained from the data. As described previously, the characteristic has three stages, the top and bottom saturation stages and the gain stage. As expected, due to different DAC voltages, the four input-output characteristics exhibit different slopes; the higher polarisation has the higher gain, whereas the lower polarisation has the lower gain. Instead, Figure 4.10b shows the change of resistance of the four sensors; as expected, the resistance and its variation

decrease with higher weights.

Sensitivity in different zones of the tile
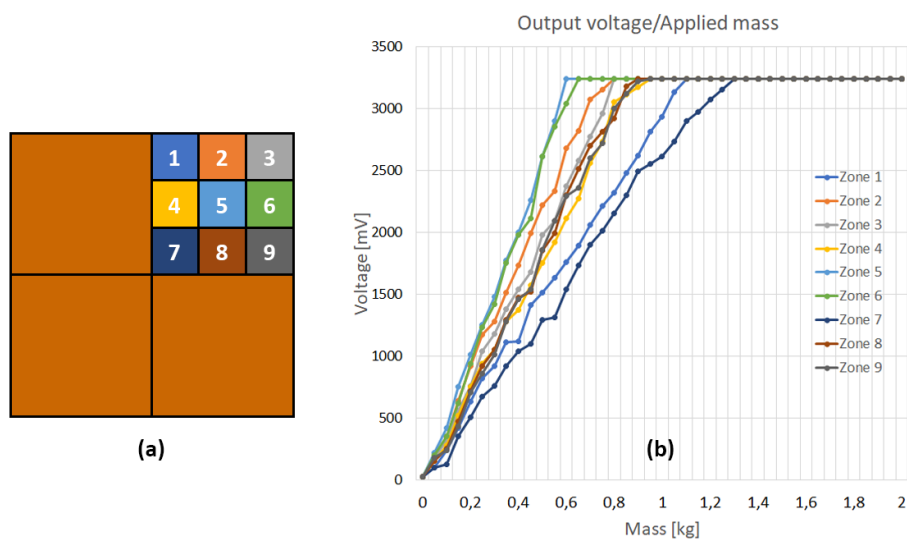
Figure 4.11: **(a)** The division of the smart tile used to assess the sensitivity in one of its quarters. **(b)** The output voltages of the conditioning circuits with a mass positioned on a specific zone.

To evaluate the smart tile sensitivity, we made a series of experimental measures described in the following. The first measures tried to identify the sensitivity in the proximity of one sensor; in this regard, we divided one-quarter of the tile into nine zones (Figure 4.11a), over which the weight was incrementally applied with steps of 50 grams while measuring the conditioning circuits outputs. The measures were taken for each quarter, providing similar results.

The results are shown in Figure 4.11b (the colours of the lines in Figure 4.11b match the zones' colours in Figure 4.11a). As expected, the output values increased with the weight increments. The results show a dependency of the circuit response due to the zone over which the mass was applied. Indeed, the curve with the higher slope

is relative to zone number 5, the zone under which the sensor was placed. Moreover, after the tile centre, the higher slopes are provided by the zones on the borders (zones 6, 2 and 3). Such behaviour is due to the reduced directions over which the force can propagate; indeed, for the zones closer to the tile's centre (zone 7, for example), the force is distributed over more directions, thus reducing the pressure on the sensor. The results also show that the smart tile can produce a significant output change for a mass of 300 grams (we consider significant a change of at least 500 mV).
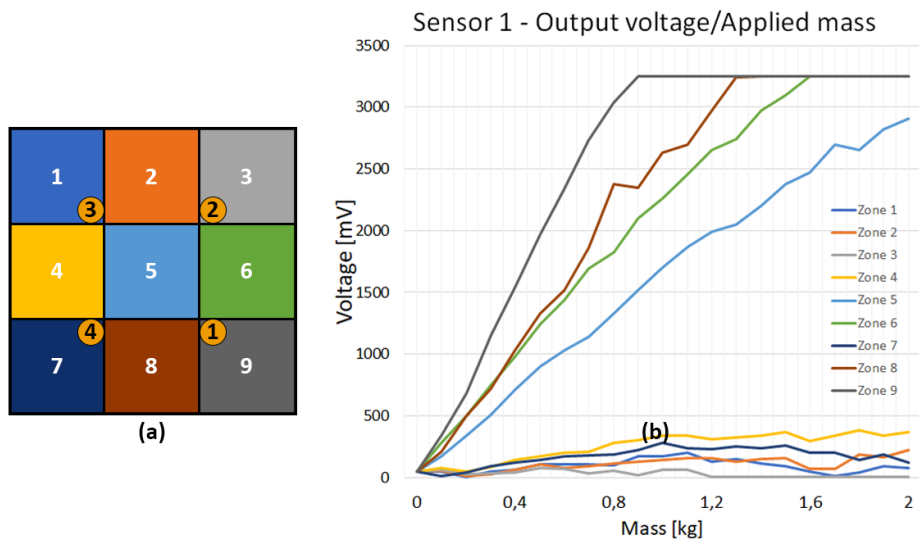
Figure 4.12: **(a)** The division of the smart tile used to assess its sensitivity to weights **(b)** The response of the conditioning circuits when a mass is positioned over a specific zone of the smart tile.

The same process was applied for the successive measures, which involved the tile in its entirety. The new subdivision of the smart tile, together with the sensors' position, is shown in Figure 4.12a, while the outputs of the conditioning circuit of sensor number one are displayed in Figure 4.12b (again the zones' colours and the lines' colours match). Those experimental measures allowed us to verify the sensitivity over a larger surface. We measured the circuit response to weight increments of 100 grams.

The results show that a 300 grams sensitivity is obtainable only for four zones over nine; indeed, the value of 500 mV is reached only by four lines in Figure 4.12b. Such an event is explainable considering the distance of the zones from the sensor. Zone 9 is the one that provides the higher increase because the sensor is positioned under it. Zones number 8, 6, and 5 are the closest to sensor number one, thus the others that show an output increase. The remaining zones are too distant to provide a valuable increase even for a mass of 2 kilograms. The results suggest that it is mandatory to use at least four sensors to have the required sensitivity over the entire surface. The other sensors provide similar results.

Chapter 5

Discussion, future developments and conclusions

In this chapter, final comments about the two systems will be reported. The discussion starts with the BCG/SCG system and continues with the smart floor system. Such discussions contain a comparison with the literature, a summary of the results and the future development necessary to improve the technologies.

5.1 Discussion on the BCG and SCG system

In Chapters 2 and 4, we have discussed the technical aspects, the methodology and the results of the BCG and SCG system. The following paragraphs compare such results and methods with other works in literature.

Regarding the SCG system, it should be underlined that various papers focused on the identification of heartbeats. Authors of [127] developed an automated methodology to detect AO instants, using wavelet decomposition and Shannon energy-based detectors, achieving scores of sensitivity and precision of 94% and 90%, respectively. Only a portion of the CEBS database (SCG-2 dataset) was analysed, particularly 4585 heartbeats, approximately 6.5% of the entire database. During the analysis of database SCG-2, our methodology discarded no beats, achieving higher perfor-

mances. Even if our method does not search for AO instants but the simple presence of a heartbeat, it is worth comparing the results.

Instead, through a moving average methodology, the authors of reference [128] discuss a way to identify systolic and diastolic regions in the SCG through a moving average method. Authors report 4% and 9% errors for detecting systole and diastole events, respectively; our results favourably compare.

To test their methodology, the authors of reference [129] acquired SCG and ECG signals during a Lower Body Negative Pressure (LBNP) test with participants positioned supine. They obtained a beat detection average sensitivity to increasing lower body negative pressure levels of 97.2%, 93.0%, 76.9%, 61.6%, 65.0%, whereas RMSE values are 40, 71, 26, 51, and 27 ms. Even authors of [130] acquired and analysed a dataset with the subjects in the LBNP condition, declaring an annotation error of 9±9 ms (mean ±standard deviation).

Through accelerometer and gyroscope, the authors of [131] designed a methodology able to reach high performances. Indeed, sensitivity and precision reached 99.9% and 99.6%, respectively. Instead, the RMSE reached 5.6 ms, with signals sampled at a frequency of 800 Hz. In the case of the SCG-2 dataset, our algorithm achieved an RMSE of 4.5 ms with a similar sampling frequency (500 Hz). Conversely, in [46], a very low RMSE was achieved, with a detection rate range of 32% - 14%.

Using a smartphone, the authors of [132] acquired eleven SCG traces; through continuous wavelet transform, they analyse the signals and obtain a sensitivity of 99.5% and precision of 97.4%. Even though such scores are comparable to ours, the beat-to-beat errors have a standard deviation of around 17.5 ms, higher than any value obtained in the datasets we have analysed.

In [133], the authors train different machine learning algorithms to detect heartbeats inside a portion of the CEBS database (SCG-2 dataset). The models are trained on 6000 cardiac cycles and cross-validated on 3000 (whereas the CEBS database contains approximately 69,500 beats, all analysed in our methodology). Initially, the traces are segmented using the ECG trace to identify the regions of interest; successively, authors use a series of binary classifications to annotate different maxima. The best average sensitivity and precision results are around 97% and 95%, respec-

tively. Instead, the best RMSE error is 3.2 ms, although such a result is obtained having as reference the R peak; instead, our results are computed between consecutive annotations. Such difference implies a factor of $\sqrt{2}$ in favour of the former (i.e. $RMSE_{C-C} \approx \sqrt{2} \cdot RMSE_{R-C}$). Such implication indicates that our methods provide slightly better scores while considering the entire CEBS database. Moreover, our results were obtained without supervision, thus without ECG information.

Regarding BCG, the scores obtained compare correctly with other works in the literature. In [121], the authors compare setups differentiating between single/double bed, sex, and sensor type, achieving a MAE of 13.22 ms with a sampling frequency of 300 Hz. Instead, reference [134] reports a MAE of 7.7 ms for an analysis computed over BCG signals acquired from a smart chair. A similar setup was used in reference [135] with a sampling frequency of 1k Hz; the authors declare a standard deviation of the measurement errors of 14.35 ms, a value superior to each 10_{th} LPP of our RMSE's results. Also, the proposed methodology compares well with the scores of [121] and [134]. Indeed, the MAE reported in the former is above the 10_{th} LPP of dataset BCG-1, whereas in [134] the MAE is close to such value.

Taking into account sensitivity, the authors of [136] scored 92.7%. Instead, reference [121] reports a precision of 98.8%, a value comparable to ours. The best-performing method described in reference [137] achieved a 95.0% sensitivity, a lower value if compared to our methodology.

Our methodology well compares with the literature for both SCG and BCG signals. Although a good concordance with the literature, the work presented here has its limitations:

- The datasets analysed provide signals from static or quasi-static conditions. However, motion artefact-free periods are present during an ordinary day, like during sleep, especially for senior users.

- Future developments will add new features to our methodology. For example, from a perspective of a stand-alone device, it is necessary to discriminate between quiet periods and motion-intensive ones.

- BCG signals, in particular, can be acquired through different objects, which

influence the output signals. It is important to study such influences to reduce them. As an initial step toward such understanding, we want to compare the quality of the BCG signals obtained from different locations under the bed through a second accelerometer.

- A design of a stand-alone device will need further studies on power consumption and computational demand, two fundamental aspects necessary to provide a suitable device. Moreover, the analysis algorithm must be adapted to an embedded solution reducing the time range of the analysis to a few heartbeats.

- The signals analysed were obtained in laboratory conditions. Future developments will investigate signals provided by domestic environments. We have already acquired and analysed a six-hour measure, and the results are promising. Data were obtained from one subject while sleeping at night; results aligned with the scores precedently discussed. However, we discarded approximately 2% of the data due to motion corruption of the ECG, which made BCG validation impossible. We achieved a 95.4% sensitivity and a 94.8% precision on the valid data, with RMSE and MAE of 5.12 and 3.54 ms, respectively.

5.2   Discussion on the smart floor system

In Chapter 3, we have presented and described a smart floor system. The following paragraphs contain a brief discussion of the main features of such a system.

We focused on creating a device that can engage users of different generations and stimulate active behaviour. Such involvement can only happen with a responsive device for good user interaction; the strict requirements and the methodology of games' design came from this necessity. The experimental measures conducted above the smart tile show the achievement of the requirements. In particular, we have designed a smart floor sensible to the touch of children's hands or feet.

Compared to other works in literature [138, 139], our system provides more than a smart floor for activity detection, adding a ludic feature. Moreover, some design choices like the anti-trauma material and future engineering will allow the system to

be displaced outdoor. While also other studies [107] investigated a modular system able to be an entertainment platform, the outdoor component can bring a different perspective to such a device.

The device has been tested and presented in public on multiple occasions; users always provided positive feedback from its use. Surveys conducted among the users are promising and indicate that the system can achieve its purposes. Future developments will be directed in various paths:

- The user interaction can be improved by adding, for example, sound outputs and new inputs like buttons or displays.

- The limited choice of games is an obstacle to the purposes of the system. Adding a more extensive availability of games is desirable.

- Some technical limitations need to be addressed to improve the system quality. For example, power consumption should be limited; moreover, in the perspective of outdoor use, the system must be engineered to be impermeable.

- We identified some problems in the sensing of pressures when the smart tiles are not mechanically blocked. The study of an improved mechanical structure can reduce them.

- New materials must be studied for indoor use, like ceramics or wood.

5.3 Conclusions

The work described in this document focused on the study and the design of systems that can provide a better life to users by identifying possible problems and stimulating more active behaviours. The former is the purpose of the BCG and SCG system, while the latter is the purpose of the smart floor system.

The first system allows the acquisition and analysis of BCG and SCG waveforms. The system's principal elements and features were described as the algorithmic phases that bring heartbeats detection.

We tested our methodology on four different datasets, two containing SCG traces and two containing BCG traces from bed setups. The databases differ in multiple aspects like measurement protocol, subjects involved, time resolution and many more. Such differences allow exploring and testing the system in various scenarios.

The performances measured are stable across all the datasets; we have validated this characteristic through statistical tests performed over precision and sensitivity scores. Instead, the same tests were conducted over RMSE and MAE scores, showing a dependency between such results and the sampling frequency. Lower frequencies provide higher values; thus, less efficiency in precise time annotation because of a less fine temporal resolution. Such limitation imposes to choose between power savings and temporal resolution.

A unified methodology for SCG and BCG analysis does not imply any performances loss. Indeed, comparisons with other works in the literature show that the proposed method can often provide better results. Future developments will need to adapt the algorithm to an embedded implementation by reducing the temporal range of analysis to a few heartbeats.

The second system is a 4 meters large and 2 meters long smart floor that can interact with the users to recognise activities and stimulate healthy behaviours through various games. The device was designed in the context of the project PLEINAIR, which Regione Emilia-Romagna founds.

We connected 32 smart tiles mechanically and electrically to create the smart floor. The smart tiles have a mechanical structure that we expressly designed to be functional and straightforward. The main elements of the mechanical system are an anti-trauma tile, piezoresistive sensors, LEDs, and PVC layers. The control of the smart floor is made through different electronic boards named RIO, which acquire the signals, light up the LEDs and provide information on activity to a controller board through an I^2C bus. The controller board elaborates the data, commands the RIO boards and transmits the results to a server through Wi-Fi.

We designed the RIO board to meet our requirements, particularly the conditioning circuit, which must sense a mass of 300 grams. Measures taken on the conditioning circuit shows the validity of the solution adopted and suggest the minimum number

of sensors to use to respect the requirements in the entire tile surface.

Two procedures must end correctly to start the smart floor and make it operate properly: the discovery and calibration procedures. The first allows the controller to know the spatial positioning of each tile, while the second one allows the calibration of all the sensors.

Each game developed was first described using a state machine and successively translated into C code. Such methodology allowed to reduce possible errors and undesired behaviours of the floor.

The system was presented to the public on multiple occasions, always receiving positive feedback and appreciation.

The two systems were designed to work independently, but a great value could come by fusing their information. Indeed, introducing such systems (opportunely adapted) in a domestic environment allows access to physiological data and activity monitoring together. In such a context, analysis to discover possible anomalies, trends and problems can become easier due to the richness of the data.

Bibliography

[1] Max Roser, Esteban Ortiz-Ospina, and Hannah Ritchie. Life expectancy. *Our World in Data*, 2013. https://ourworldindata.org/life-expectancy.

[2] Jennifer L. Rodgers, Jarrod Jones, Samuel I. Bolleddu, Sahit Vanthenapalli, Lydia E. Rodgers, Kinjal Shah, Krishna Karia, and Siva K. Panguluri. Cardiovascular Risks Associated with Gender and Aging. *Journal of Cardiovascular Development and Disease*, 6(2):19, apr 2019.

[3] Pekka Jousilahti, Erkki Vartiainen, Jaakko Tuomilehto, and Pekka Puska. Sex, Age, Cardiovascular Risk Factors, and Coronary Heart Disease. *Circulation*, 99(9):1165–1172, mar 1999.

[4] Emelia J. Benjamin, Salim S. Virani, Clifton W. Callaway, Alanna M. Chamberlain, Alexander R. Chang, Susan Cheng, Stephanie E. Chiuve, Mary Cushman, Francesca N. Delling, Rajat Deo, Sarah D. de Ferranti, Jane F. Ferguson, Myriam Fornage, Cathleen Gillespie, Carmen R. Isasi, Monik C. Jiménez, Lori C. Jordan, Suzanne E. Judd, Daniel Lackland, Judith H. Lichtman, Lynda Lisabeth, Simin Liu, Chris T. Longenecker, Pamela L. Lutsey, Jason S. Mackey, David B. Matchar, Kunihiro Matsushita, Michael E. Mussolino, Khurram Nasir, Martin O'Flaherty, Latha P. Palaniappan, Ambarish Pandey, Dilip K. Pandey, Mathew J. Reeves, Matthew D. Ritchey, Carlos J. Rodriguez, Gregory A. Roth, Wayne D. Rosamond, Uchechukwu K. A. Sampson, Gary M. Satou, Svati H. Shah, Nicole L. Spartano, David L. Tirschwell, Connie W. Tsao, Jenifer H. Voeks, Joshua Z. Willey, John T. Wilkins, Jason HY.

Wu, Heather M. Alger, Sally S. Wong, and Paul Muntner. Heart Disease and Stroke Statistics—2018 Update: A Report From the American Heart Association. *Circulation*, 137(12), mar 2018.

[5] Harold W. Kohl. Physical activity and cardiovascular disease: evidence for a dose response. *Medicine and Science in Sports and Exercise*, 33(Supplement):S472–S483, jun 2001.

[6] Matthew A. Nystoriak and Aruni Bhatnagar. Cardiovascular Effects and Benefits of Exercise. *Frontiers in Cardiovascular Medicine*, 5, sep 2018.

[7] Yitong Huang, Steve Benford, Dominic Price, Roma Patel, Benqian Li, Alex Ivanov, and Holly Blake. Using Internet of Things to Reduce Office Workers' Sedentary Behavior: Intervention Development Applying the Behavior Change Wheel and Human-Centered Design Approach. *JMIR mHealth and uHealth*, 8(7):e17914, jul 2020.

[8] Franco van Wyk, Anahita Khojandi, Brian Williams, Don MacMillan, Robert L. Davis, Daniel A. Jacobson, and Rishikesan Kamaleswaran. A Cost-Benefit Analysis of Automated Physiological Data Acquisition Systems Using Data-Driven Modeling. *Journal of Healthcare Informatics Research*, 3(2):245–263, jun 2019.

[9] Bruce Del Mar. The history of clinical holter monitoring. *Annals of Noninvasive Electrocardiology*, 10(2):226–230, April 2005.

[10] Jiangqi Zhao, Yuanjing Lin, Jingbo Wu, Hnin Y. Y. Nyein, Mallika Bariya, Li-Chia Tai, Minghan Chao, Wenbo Ji, George Zhang, Zhiyong Fan, and Ali Javey. A Fully Integrated and Self-Powered Smartwatch for Continuous Sweat Glucose Monitoring. *ACS Sensors*, 4(7):1925–1933, jul 2019.

[11] Pekka Siirtola. Continuous stress detection using the sensors of commercial smartwatch. In *Adjunct Proceedings of the 2019 ACM International Joint Conference on Pervasive and Ubiquitous Computing and Proceedings of the*

2019 ACM International Symposium on Wearable Computers, pages 1198–1201, New York, NY, USA, sep 2019. ACM.

[12] Rohit M. Panicker and Baskaran Chandrasekaran. "Wearables on vogue": a scoping review on wearables on physical activity and sedentary behavior during COVID-19 pandemic. *Sport Sciences for Health*, jan 2022.

[13] Diana Yacchirema, Jara Suárez de Puga, Carlos Palau, and Manuel Esteve. Fall detection system for elderly people using IoT and Big Data. *Procedia Computer Science*, 130:603–610, 2018.

[14] PLEINAIR Official website - https://www.pleinairpark.it/.

[15] PLEINAIR partners list - https://www.pleinairpark.it/partner-imprese-pleinair/.

[16] Isabel de la Torre-Díez, Miguel López-Coronado, Cesar Vaca, Jesús S. Aguado, and Carlos de Castro. Cost-Utility and Cost-Effectiveness Studies of Telemedicine, Electronic, and Mobile Health Systems in the Literature: A Systematic Review. *Telemedicine and e-Health*, 21(2):81–85, feb 2015.

[17] Niccolò Mora, Guido Matrella, and Paolo Ciampolini. Cloud-Based Behavioral Monitoring in Smart Homes. *Sensors*, 18(6):1951, jun 2018.

[18] Niccolò Mora, Ilaria De Munari, and Paolo Ciampolini. Subject-independent, SSVEP-based BCI: Trading off among accuracy, responsiveness and complexity. In *2015 7th International IEEE/EMBS Conference on Neural Engineering (NER)*, pages 146–149. IEEE, apr 2015.

[19] Derek K. Ho. Voice-controlled virtual assistants for the older people with visual impairment. *Eye*, 32(1):53–54, jan 2018.

[20] Aleksandra Stojanova, Saso Koceski, and Natasa Koceska. Continuous Blood Pressure Monitoring as a Basis for Ambient Assisted Living (AAL) – Review of Methodologies and Devices. *Journal of Medical Systems*, 43(2):24, feb 2019.

[21] James D. Amor and Christopher J. James. Validation of a Commercial Android Smartwatch as an Activity Monitoring Platform. *IEEE Journal of Biomedical and Health Informatics*, 22(4):968–978, jul 2018.

[22] Youngsun Kong and Ki H. Chon. Heart Rate Tracking Using a Wearable Photoplethysmographic Sensor During Treadmill Exercise. *IEEE Access*, 7:152421–152428, 2019.

[23] Linda M. Eerikäinen, Alberto G. Bonomi, Fons Schipper, Lukas Dekker, Rik Vullings, Helma M. de Morree, and Ronald M. Aarts. How accurately can we detect atrial fibrillation using photoplethysmography data measured in daily life? In *2019 Computing in Cardiology (CinC)*, pages Page 1–Page 4, 2019.

[24] Christina Hahnen, Cecilia G. Freeman, Nilanjan Haldar, Jacquelyn N. Hamati, Dylan M. Bard, Vignesh Murali, Geno J. Merli, Jeffrey I. Joseph, and Noud van Helmond. Accuracy of Vital Signs Measurements by a Smartwatch and a Portable Health Device: Validation Study. *JMIR mHealth and uHealth*, 8(2):e16811, feb 2020.

[25] Hussein Al Osman, Mohamad Eid, and Abdulmotaleb El Saddik. A Pattern-Based Windowed Impulse Rejection Filter for Nonpathological HRV Artifacts Correction. *IEEE Transactions on Instrumentation and Measurement*, 64(7):1944–1957, jul 2015.

[26] Chavdar Levkov, Georgy Mihov, Ratcho Ivanov, Ivan Daskalov, Ivaylo Christov, and Ivan Dotsinsky. Removal of power-line interference from the ECG: a review of the subtraction procedure. *BioMedical Engineering OnLine*, 4(1):50, dec 2005.

[27] Sucharita Mitra, Madhuchhanda Mitra, and Bidyut B. Chaudhuri. A Rough-Set-Based Inference Engine for ECG Classification. *IEEE Transactions on Instrumentation and Measurement*, 55(6):2198–2206, dec 2006.

[28] Masahiro Inoue, Yusaku Amano, and Yasunori Tada. Design of printed E-textile probers to supress electrocardiograpy noise. In *2017 International Conference on Electronics Packaging (ICEP)*, pages 464–465. IEEE, apr 2017.

[29] Ana Mincholé and Blanca Rodriguez. Artificial intelligence for the electrocardiogram. *Nature Medicine*, 25(1):22–23, jan 2019.

[30] Qingxue Zhang, Dian Zhou, and Xuan Zeng. HeartID: A Multiresolution Convolutional Neural Network for ECG-Based Biometric Human Identification in Smart Health Applications. *IEEE Access*, 5:11805–11816, 2017.

[31] Mohamad Forouzanfar, Saif Ahmad, Izmail Batkin, Hilmi R. Dajani, Voicu Z. Groza, and Miodrag Bolic. Model-Based Mean Arterial Pressure Estimation Using Simultaneous Electrocardiogram and Oscillometric Blood Pressure Measurements. *IEEE Transactions on Instrumentation and Measurement*, 64(9):2443–2452, sep 2015.

[32] Kurt Barbe, Wendy Van Moer, and Danny Schoors. Analyzing the Windkessel Model as a Potential Candidate for Correcting Oscillometric Blood-Pressure Measurements. *IEEE Transactions on Instrumentation and Measurement*, 61(2):411–418, feb 2012.

[33] Jiapu Pan and Willis J. Tompkins. A Real-Time QRS Detection Algorithm. *IEEE Transactions on Biomedical Engineering*, BME-32(3):230–236, mar 1985.

[34] Juan Arteaga-Falconi, Hussein Al Osman, and Abdulmotaleb El Saddik. R-peak detection algorithm based on differentiation. In *2015 IEEE 9th International Symposium on Intelligent Signal Processing (WISP) Proceedings*, pages 1–4. IEEE, may 2015.

[35] Natalia M. Arzeno, Zhi-De Deng, and Chi-Sang Poon. Analysis of First-Derivative Based QRS Detection Algorithms. *IEEE Transactions on Biomedical Engineering*, 55(2):478–484, feb 2008.

[36] Bruno Gil, Salzitsa Anastasova, and Guang Yang. A Smart Wireless Ear-Worn Device for Cardiovascular and Sweat Parameter Monitoring During Physical Exercise: Design and Performance Results. *Sensors*, 19(7):1616, apr 2019.

[37] David M. Salerno and John M. Zanetti. Seismocardiography : a new technique for recording cardiac vibrations. concept, method, and initial observations. 1990.

[38] John M. Zanetti and David M. Salerno. Seismocardiography: a technique for recording precordial acceleration. In *[1991] Computer-Based Medical Systems@m_Proceedings of the Fourth Annual IEEE Symposium*, pages 4–9, 1991.

[39] Omer T. Inan, Pierre-Francois Migeotte, Kwang-Suk Park, Mozziyar Etemadi, Kouhyar Tavakolian, Ramon Casanella, John Zanetti, Jens Tank, Irina Funtova, G. Kim Prisk, and Marco Di Rienzo. Ballistocardiography and Seismocardiography: A Review of Recent Advances. *IEEE Journal of Biomedical and Health Informatics*, 19(4):1414–1427, jul 2015.

[40] Marco Di Rienzo, Paolo Meriggi, Emanuele Vaini, Paolo Castiglioni, and Francesco Rizzo. 24h seismocardiogram monitoring in ambulant subjects. In *2012 Annual International Conference of the IEEE Engineering in Medicine and Biology Society*, pages 5050–5053. IEEE, aug 2012.

[41] Fábio Leitão, Eurico Moreira, Filipe Alves, Mário Lourenço, Olga Azevedo, João Gaspar, and Luis Rocha. High-Resolution Seismocardiogram Acquisition and Analysis System. *Sensors*, 18(10):3441, oct 2018.

[42] Marco Di Rienzo, Emanuele Vaini, Paolo Castiglioni, Prospero Lombardi, Paolo Meriggi, and Francesco Rizzo. A textile-based wearable system for the prolonged assessment of cardiac mechanics in daily life. In *2014 36th Annual International Conference of the IEEE Engineering in Medicine and Biology Society*, pages 6896–6898. IEEE, aug 2014.

[43] Amirtahà Taebi, Brian Solar, Andrew Bomar, Richard Sandler, and Hansen Mansy. Recent Advances in Seismocardiography. *Vibration*, 2(1):64–86, jan 2019.

[44] Ghufran Shafiq, Sivanagaraja Tatinati, Wei Tech Ang, and Kalyana C. Veluvolu. Automatic Identification of Systolic Time Intervals in Seismocardiogram. *Scientific Reports*, 6(1):37524, dec 2016.

[45] Niccolo Mora, Federico Cocconcelli, Guido Matrella, and Paolo Ciampolini. Fully Automated Annotation of Seismocardiogram for Noninvasive Vital Sign Measurements. *IEEE Transactions on Instrumentation and Measurement*, 69(4):1241–1250, apr 2020.

[46] Farzad Khosrow-Khavar, Kouhyar Tavakolian, Andrew Blaber, and Carlo Menon. Automatic and Robust Delineation of the Fiducial Points of the Seismocardiogram Signal for Noninvasive Estimation of Cardiac Time Intervals. *IEEE Transactions on Biomedical Engineering*, 64(8):1701–1710, aug 2017.

[47] Kasper Sørensen, Samuel E. Schmidt, Ask S. Jensen, Peter Søgaard, and Johannes J. Struijk. Definition of Fiducial Points in the Normal Seismocardiogram. *Scientific Reports*, 8(1):15455, dec 2018.

[48] Richard S. Crow, Peter Hannan, David Jacobs, Lowell Hedquist, and David M. Salerno. Relationship between Seismocardiogram and Echocardiogram for Events in the Cardiac Cycle. *American Journal of Noninvasive Cardiology*, 8(1):39–46, 1994.

[49] Farzad Khosrow-khavar, Kouhyar Tavakolian, Andrew P. Blaber, John M. Zanetti, Reza Fazel-Rezai, and Carlo Menon. Automatic Annotation of Seismocardiogram With High-Frequency Precordial Accelerations. *IEEE Journal of Biomedical and Health Informatics*, 19(4):1428–1434, jul 2015.

[50] Tero Hurnanen, Eero Lehtonen, Mojtaba J. Tadi, Tom Kuusela, Tuomas Kiviniemi, Antti Saraste, Tuija Vasankari, Juhani Airaksinen, Tero Koivisto,

and Mikko Pankaala. Automated Detection of Atrial Fibrillation Based on Time–Frequency Analysis of Seismocardiograms. *IEEE Journal of Biomedical and Health Informatics*, 21(5):1233–1241, sep 2017.

[51] Niccolò Mora, Federico Cocconcelli, Guido Matrella, and Paolo Ciampolini. Detection and Analysis of Heartbeats in Seismocardiogram Signals. *Sensors*, 20(6):1670, mar 2020.

[52] Omer T. Inan, Maziyar Baran Pouyan, Abdul Q. Javaid, Sean Dowling, Mozziyar Etemadi, Alexis Dorier, J. Alex Heller, A. Ozan Bicen, Shuvo Roy, Teresa De Marco, and Liviu Klein. Novel Wearable Seismocardiography and Machine Learning Algorithms Can Assess Clinical Status of Heart Failure Patients. *Circulation: Heart Failure*, 11(1), jan 2018.

[53] Mojtaba Jafari Tadi, Eero Lehtonen, Antti Saraste, Jarno Tuominen, Juho Koskinen, Mika Teräs, Juhani Airaksinen, Mikko Pänkäälä, and Tero Koivisto. Gyrocardiography: A New Non-invasive Monitoring Method for the Assessment of Cardiac Mechanics and the Estimation of Hemodynamic Variables. *Scientific Reports*, 7(1):6823, dec 2017.

[54] Chenxi Yang, Sunli Tang, and Negar Tavassolian. Utilizing Gyroscopes Towards the Automatic Annotation of Seismocardiograms. *IEEE Sensors Journal*, 17(7):2129–2136, apr 2017.

[55] Matti Kaisti, Mojtaba J. Tadi, Olli Lahdenoja, Tero Hurnanen, Antti Saraste, Mikko Pankaala, and Tero Koivisto. Stand-Alone Heartbeat Detection in Multidimensional Mechanocardiograms. *IEEE Sensors Journal*, 19(1):234–242, jan 2019.

[56] Olli Lahdenoja, Mikko Pankaala, Tero Koivisto, Tero Hurnanen, Zuhair Iftikhar, Sami Nieminen, Timo Knuutila, Antti Saraste, Tuomas Kiviniemi, Tuija Vasankari, and Juhani Airaksinen. Atrial Fibrillation Detection via Accelerometer and Gyroscope of a Smartphone. *IEEE Journal of Biomedical and Health Informatics*, 22(1):108–118, jan 2018.

[57] Chenxi Yang and Negar Tavassolian. Combined Seismo- and Gyro-Cardiography: A More Comprehensive Evaluation of Heart-Induced Chest Vibrations. *IEEE Journal of Biomedical and Health Informatics*, 22(5):1466–1475, sep 2018.

[58] Chenxi Yang and Negar Tavassolian. An Independent Component Analysis Approach to Motion Noise Cancelation of Cardio-Mechanical Signals. *IEEE Transactions on Biomedical Engineering*, 66(3):784–793, mar 2019.

[59] Aditya Sundar and Vivek Pahwa. Evaluating the Performance of State of the Art Algorithms for Enhancement of Seismocardiogram Signals. In *Proceedings of the First International Conference on Intelligent Computing and Communication*, pages 37–45. 2017.

[60] Abdul Q. Javaid, Hazar Ashouri, Alexis Dorier, Mozziyar Etemadi, J. Alex Heller, Shuvo Roy, and Omer T. Inan. Quantifying and Reducing Motion Artifacts in Wearable Seismocardiogram Measurements During Walking to Assess Left Ventricular Health. *IEEE Transactions on Biomedical Engineering*, 64(6):1277–1286, jun 2017.

[61] Isaac Starr. The relation of the ballistocardiogram to cardiac function. *The American Journal of Cardiology*, 2(6):737–747, dec 1958.

[62] Ibrahim Sadek, Jit Biswas, and Bessam Abdulrazak. Ballistocardiogram signal processing: a review. *Health Information Science and Systems*, 7(1):10, dec 2019.

[63] Peyman Yousefian, Sungtae Shin, Azin Mousavi, Chang-Sei Kim, Ramakrishna Mukkamala, Dae-Geun Jang, Byung-Hoon Ko, Jongwook Lee, Ui K. Kwon, Youn H. Kim, and Jin-Oh Hahn. The Potential of Wearable Limb Ballistocardiogram in Blood Pressure Monitoring via Pulse Transit Time. *Scientific Reports*, 9(1):10666, dec 2019.

[64] Andrew D. Wiens, Ann Johnson, and Omer T. Inan. Wearable Sensing of Cardiac Timing Intervals From Cardiogenic Limb Vibration Signals. *IEEE Sensors Journal*, 17(5):1463–1470, mar 2017.

[65] Katy Lydon, Bo Yu Su, Licet Rosales, Moein Enayati, Kenneth C. Ho, Marilyn Rantz, and Marjorie Skubic. Robust heartbeat detection from in-home ballistocardiogram signals of older adults using a bed sensor. In *2015 37th Annual International Conference of the IEEE Engineering in Medicine and Biology Society (EMBC)*, pages 7175–7179. IEEE, aug 2015.

[66] Rafael González-Landaeta, Oscar Casas, and Ramon Pallàs-Areny. Heart rate detection from an electronic weighing scale. *Physiological Measurement*, 29(8):979–988, aug 2008.

[67] Teemu Koivistoinen, Sakari Junnila, Alpo Varri, and Tiit Koobi. A new method for measuring the ballistocardiogram using EMFi sensors in a normal chair. In *The 26th Annual International Conference of the IEEE Engineering in Medicine and Biology Society*, volume 3, pages 2026–2029. IEEE.

[68] Niccolò Mora, Federico Cocconcelli, Guido Matrella, and Paolo Ciampolini. A Unified Methodology for Heartbeats Detection in Seismocardiogram and Ballistocardiogram Signals. *Computers*, 9(2):41, may 2020.

[69] Chang-Sei Kim, Andrew M. Carek, Omer T. Inan, Ramakrishna Mukkamala, and Jin-Oh Hahn. Ballistocardiogram-Based Approach to Cuffless Blood Pressure Monitoring: Proof of Concept and Potential Challenges. *IEEE Transactions on Biomedical Engineering*, 65(11):2384–2391, nov 2018.

[70] Jianwei Su, Xuezhou Zhu, Xiaodong Zhang, Jintian Tang, and Lei Liu. Ballistocardiogram Measurement System Using Three Load-Cell Sensors Platform in Chair. In *2009 2nd International Conference on Biomedical Engineering and Informatics*, pages 1–4. IEEE, 2009.

[71] Juha M. Kortelainen, Mark van Gils, and Juha Pärkkä. Multichannel bed pressure sensor for sleep monitoring. In *2012 Computing in Cardiology*, pages 313–316, 2012.

[72] Mariusz Krej, Lukasz Dziuda, and Franciszek W. Skibniewski. A Method of Detecting Heartbeat Locations in the Ballistocardiographic Signal From the Fiber-Optic Vital Signs Sensor. *IEEE Journal of Biomedical and Health Informatics*, 19(4):1443–1450, jul 2015.

[73] Weimin Lyu, Wei Xu, Fangang Yang, Shuyang Chen, Fengze Tan, and Changyuan Yu. Non-Invasive Measurement for Cardiac Variations Using a Fiber Optic Sensor. *IEEE Photonics Technology Letters*, 33(18):990–993, sep 2021.

[74] Dangdang Shao, Francis Tsow, Chenbin Liu, Yuting Yang, and Nongjian Tao. Simultaneous Monitoring of Ballistocardiogram and Photoplethysmogram Using a Camera. *IEEE Transactions on Biomedical Engineering*, 64(5):1003–1010, may 2017.

[75] Hyunwoo Lee, Ayoung Cho, Seongwon Lee, and Mincheol Whang. Vision-Based Measurement of Heart Rate from Ballistocardiographic Head Movements Using Unsupervised Clustering. *Sensors*, 19(15):3263, jul 2019.

[76] Giovanna Guidoboni, Lorenzo Sala, Moein Enayati, Riccardo Sacco, Marcela Szopos, James M. Keller, Mihail Popescu, Laurel Despins, Virginia H. Huxley, and Marjorie Skubic. Cardiovascular Function and Ballistocardiogram: A Relationship Interpreted via Mathematical Modeling. *IEEE Transactions on Biomedical Engineering*, 66(10):2906–2917, oct 2019.

[77] Chang-Sei Kim, Stephanie L. Ober, M. Sean McMurtry, Barry A. Finegan, Omer T. Inan, Ramakrishna Mukkamala, and Jin-Oh Hahn. Ballistocardiogram: Mechanism and Potential for Unobtrusive Cardiovascular Health Monitoring. *Scientific Reports*, 6(1):31297, nov 2016.

[78] Abdul Q. Javaid, Andrew D. Wiens, Nathaniel F. Fesmire, Mary A. Weitnauer, and Omer T. Inan. Quantifying and Reducing Posture-Dependent Distortion in Ballistocardiogram Measurements. *IEEE Journal of Biomedical and Health Informatics*, 19(5):1549–1556, sep 2015.

[79] Yang Yao, Zahra Ghasemi, Md. M. H. Shandhi, Hazar Ashouri, Lisheng Xu, Ramakrishna Mukkamala, Omer T. Inan, and Jin-Oh Hahn. Mitigation of Instrument-Dependent Variability in Ballistocardiogram Morphology: Case Study on Force Plate and Customized Weighing Scale. *IEEE Journal of Biomedical and Health Informatics*, 24(1):69–78, jan 2020.

[80] C. Brüser, Stefan Winter, and Steffen Leonhardt. Robust inter-beat interval estimation in cardiac vibration signals. *Physiological Measurement*, 34(2):123–138, feb 2013.

[81] Won Lee, Heenam Yoon, Chungmin Han, Kwang Joo, and Kwang Park. Physiological Signal Monitoring Bed for Infants Based on Load-Cell Sensors. *Sensors*, 16(3):409, mar 2016.

[82] Katy Lydon, Bo Yu Su, Licet Rosales, Moein Enayati, Kenneth C. Ho, Marilyn Rantz, and Marjorie Skubic. Robust heartbeat detection from in-home ballistocardiogram signals of older adults using a bed sensor. In *2015 37th Annual International Conference of the IEEE Engineering in Medicine and Biology Society (EMBC)*, pages 7175–7179. IEEE, aug 2015.

[83] Ahmad Suliman, Charles Carlson, Steve Warren, and David Thompson. Performance Evaluation of Processing Methods for Ballistocardiogram Peak Detection. In *2018 40th Annual International Conference of the IEEE Engineering in Medicine and Biology Society (EMBC)*, pages 502–505. IEEE, jul 2018.

[84] Ibrahim Sadek, Jit Biswas, Bessam Abdulrazak, Zhang Haihong, and Mounir Mokhtari. Continuous and unconstrained vital signs monitoring with ballistocardiogram sensors in headrest position. In *2017 IEEE EMBS International*

Conference on Biomedical & Health Informatics (BHI), pages 289–292. IEEE, 2017.

[85] Christoph Bruser, Jasper Diesel, Matthias D. H. Zink, Stefan Winter, Patrick Schauerte, and Steffen Leonhardt. Automatic Detection of Atrial Fibrillation in Cardiac Vibration Signals. *IEEE Journal of Biomedical and Health Informatics*, 17(1):162–171, jan 2013.

[86] Isaac S. Chang, Narges Armanfard, Abdul Q. Javaid, Jennifer Boger, and Alex Mihailidis. Unobtrusive Detection of Simulated Orthostatic Hypotension and Supine Hypertension Using Ballistocardiogram and Electrocardiogram of Healthy Adults. *IEEE Journal of Translational Engineering in Health and Medicine*, 6:1–13, 2018.

[87] Matthias D. Zink, Christoph Brüser, Björn-Ole Stüben, Andreas Napp, Robert Stöhr, Steffen Leonhardt, Nikolaus Marx, Karl Mischke, Jörg B. Schulz, and Johannes Schiefer. Unobtrusive Nocturnal Heartbeat Monitoring by a Ballistocardiographic Sensor in Patients with Sleep Disordered Breathing. *Scientific Reports*, 7(1):13175, dec 2017.

[88] Nemath Ahmed, Aashit Singh, Srivyshnav KS, Gulshan Kumar, Gaurav Parchani, and Vibhor Saran. Classification Of Sleep-Wake State In A Ballistocardiogram System Based On Deep Learning. nov 2020.

[89] Christoph Will, Kilin Shi, Sven Schellenberger, Tobias Steigleder, Fabian Michler, Jonas Fuchs, Robert Weigel, Christoph Ostgathe, and Alexander Koelpin. Radar-Based Heart Sound Detection. *Scientific Reports*, 8(1):11551, dec 2018.

[90] Nathan Jeger-Madiot, Jérôme Gateau, Mathias Fink, and Ros-Kiri Ing. Non-contact and through-clothing measurement of the heart rate using ultrasound vibrocardiography. *Medical Engineering & Physics*, 50:96–102, dec 2017.

[91] Mauricio Villarroel, Alessandro Guazzi, João Jorge, Sara Davis, Peter Watkinson, Gabrielle Green, Asha Shenvi, Kenny McCormick, and Lionel

Tarassenko. Continuous non-contact vital sign monitoring in neonatal intensive care unit. *Healthcare Technology Letters*, 1(3):87–91, sep 2014.

[92] Mark van Gastel, Sander Stuijk, and Gerard de Haan. New principle for measuring arterial blood oxygenation, enabling motion-robust remote monitoring. *Scientific Reports*, 6(1):38609, dec 2016.

[93] Rong-Chao Peng, Xiao-Lin Zhou, Wan-Hua Lin, and Yuan-Ting Zhang. Extraction of Heart Rate Variability from Smartphone Photoplethysmograms. *Computational and Mathematical Methods in Medicine*, 2015:1–11, 2015.

[94] Xiaochuan He, Rafik A. Goubran, and Xiaoping P. Liu. Secondary Peak Detection of PPG Signal for Continuous Cuffless Arterial Blood Pressure Measurement. *IEEE Transactions on Instrumentation and Measurement*, 63(6):1431–1439, jun 2014.

[95] Andrew M. Carek, Hewon Jung, and Omer T. Inan. A Reflective Photoplethysmogram Array and Channel Selection Algorithm for Weighing Scale Based Blood Pressure Measurement. *IEEE Sensors Journal*, 20(7):3849–3858, apr 2020.

[96] K. Venu Madhav, M. Raghu Ram, E. Hari Krishna, Nagarjuna R. Komalla, and K. Ashoka Reddy. Robust Extraction of Respiratory Activity From PPG Signals Using Modified MSPCA. *IEEE Transactions on Instrumentation and Measurement*, 62(5):1094–1106, may 2013.

[97] Thanos G. Stavropoulos, Asterios Papastergiou, Lampros Mpaltadoros, Spiros Nikolopoulos, and Ioannis Kompatsiaris. IoT Wearable Sensors and Devices in Elderly Care: A Literature Review. *Sensors*, 20(10):2826, may 2020.

[98] Vito Errico, Mariachiara Ricci, Antonio Pallotti, Franco Giannini, and Giovanni Saggio. Ambient assisted living for tetraplegic people by means of an electronic system based on a novel sensory headwear : Increased possibilities for reduced abilities. In *2018 IEEE International Symposium on Medical Measurements and Applications (MeMeA)*, pages 1–6. IEEE, jun 2018.

[99] Adriano Mancini, Emanuele Frontoni, and Primo Zingaretti. Embedded Multisensor System for Safe Point-to-Point Navigation of Impaired Users. *IEEE Transactions on Intelligent Transportation Systems*, 16(6):3543–3555, dec 2015.

[100] David Naranjo-Hernandez, Laura M. Roa, Javier Reina-Tosina, and Miguel A. Estudillo-Valderrama. SoM: A Smart Sensor for Human Activity Monitoring and Assisted Healthy Ageing. *IEEE Transactions on Biomedical Engineering*, 59(11):3177–3184, nov 2012.

[101] Zhihua Wang, Zhaochu Yang, and Tao Dong. A Review of Wearable Technologies for Elderly Care that Can Accurately Track Indoor Position, Recognize Physical Activities and Monitor Vital Signs in Real Time. *Sensors*, 17(2):341, feb 2017.

[102] Robert Radziszewski, Hubert Ngankam, Helene Pigot, Vincent Grégoire, Dominique Lorrain, and Sylvain Giroux. An ambient assisted living nighttime wandering system for elderly. In *Proceedings of the 18th International Conference on Information Integration and Web-based Applications and Services - iiWAS '16*, pages 368–374, New York, New York, USA, 2016. ACM Press.

[103] Niccolò Mora, Guido Matrella, and Paolo Ciampolini. Cloud-Based Behavioral Monitoring in Smart Homes. *Sensors*, 18(6):1951, jun 2018.

[104] Robert J. Orr and Gregory D. Abowd. The smart floor. In *CHI '00 extended abstracts on Human factors in computing systems - CHI '00*, page 275, New York, New York, USA, 2000. ACM Press.

[105] M.D. Addlesee, A. Jones, Finbarr Livesey, and Ferdinando Samaria. The ORL active floor [sensor system]. *IEEE Personal Communications*, 4(5):35–41, 1997.

[106] Renan Serra, Dominique Knittel, Pascal Di Croce, and Richard Peres. Activity Recognition With Smart Polymer Floor Sensor: Application to Human Footstep Recognition. *IEEE Sensors Journal*, 16(14):5757–5775, jul 2016.

[107] Seongju Chang, Sungil Ham, Seungbum Kim, Dongjun Suh, and Hyunseok Kim. Ubi-Floor: Design and Pilot Implementation of an Interactive Floor System. In *2010 Second International Conference on Intelligent Human-Machine Systems and Cybernetics*, pages 290–293. IEEE, aug 2010.

[108] Nathaniel Faulkner, Baden Parr, Fakhrul Alam, Mathew Legg, and Serge Demidenko. CapLoc: Capacitive Sensing Floor for Device-Free Localization and Fall Detection. *IEEE Access*, 8:187353–187364, 2020.

[109] Atika Arshad, Sheroz Khan, A H M Zahirul Alam, Ahmad F. Ismail, and Rumana Tasnim. Capacitive proximity floor sensing system for elderly tracking and fall detection. In *2017 IEEE 4th International Conference on Smart Instrumentation, Measurement and Application (ICSIMA)*, pages 1–5. IEEE, nov 2017.

[110] Guodong Feng, Yuebin Yang, Xuemei Guo, and Guoli Wang. A Smart Fiber Floor for Indoor Target Localization. *IEEE Pervasive Computing*, 14(2):52–59, apr 2015.

[111] Ibrahim Al-Naimi, Wong Chi Biu, Philip Moore, and Chen Xi. Advanced approach for indoor identification and tracking using smart floor and pyroelectric infrared sensors. In *2014 5th International Conference on Information and Communication Systems (ICICS)*, pages 1–6, 2014.

[112] Macarena Espinilla, Javier Medina, and Chris Nugent. UCAmI Cup. Analyzing the UJA Human Activity Recognition Dataset of Activities of Daily Living. *Proceedings*, 2(19):1267, oct 2018.

[113] Antonio Jiménez and Fernando Seco. Event-Driven Real-Time Location-Aware Activity Recognition in AAL Scenarios. *Proceedings*, 2(19):1240, oct 2018.

[114] Jesús D. Cerón, Diego M. López, and Bjoern M. Eskofier. Human Activity Recognition Using Binary Sensors, BLE Beacons, an Intelligent Floor and

Acceleration Data: A Machine Learning Approach. *Proceedings*, 2(19):1265, oct 2018.

[115] Amaya Arcelus, Christophe L. Herry, Rafik A. Goubran, Frank Knoefel, Heidi Sveistrup, and Martin Bilodeau. Determination of Sit-to-Stand Transfer Duration Using Bed and Floor Pressure Sequences. *IEEE Transactions on Biomedical Engineering*, 56(10):2485–2492, oct 2009.

[116] Federico Cocconcelli, Niccolo Mora, Guido Matrella, and Paolo Ciampolini. High-Accuracy, Unsupervised Annotation of Seismocardiogram Traces for Heart Rate Monitoring. *IEEE Transactions on Instrumentation and Measurement*, 69(9):6372–6380, sep 2020.

[117] Federico Cocconcelli, Niccolo Mora, Guido Matrella, and Paolo Ciampolini. Seismocardiography-based detection of heartbeats for continuous monitoring of vital signs. In *2019 11th Computer Science and Electronic Engineering (CEEC)*, pages 53–58. IEEE, sep 2019.

[118] Niccolo Mora, Federico Cocconcelli, Guido Matrella, and Paolo Ciampolini. Accurate Heartbeat Detection on Ballistocardiogram Accelerometric Traces. *IEEE Transactions on Instrumentation and Measurement*, 69(11):9000–9009, nov 2020.

[119] Niccolo Mora, Federico Cocconcelli, Guido Matrella, Giovanni Chiorboli, and Paolo Ciampolini. An accurate and stable bed-based ballistocardiogram measurement and analysis system. In *2021 IEEE International Workshop on Metrology for Industry 4.0 & IoT (MetroInd4.0&IoT)*, pages 482–487. IEEE, jun 2021.

[120] Ghufran Shafiq, Sivanagaraja Tatinati, Wei T. Ang, and Kalyana C. Veluvolu. Automatic Identification of Systolic Time Intervals in Seismocardiogram. *Scientific Reports*, 6(1):37524, dec 2016.

[121] Joonas Paalasmaa, Hannu Toivonen, and Markku Partinen. Adaptive Heartbeat Modeling for Beat-to-Beat Heart Rate Measurement in Ballistocardiograms.

IEEE Journal of Biomedical and Health Informatics, 19(6):1945–1952, nov 2015.

[122] Omer T. Inan, Pierre-Francois Migeotte, Kwang-Suk Park, Mozziyar Etemadi, Kouhyar Tavakolian, Ramon Casanella, John Zanetti, Jens Tank, Irina Funtova, G. Kim Prisk, and Marco Di Rienzo. Ballistocardiography and Seismocardiography: A Review of Recent Advances. *IEEE Journal of Biomedical and Health Informatics*, 19(4):1414–1427, jul 2015.

[123] Omer T. Inan, M. Etemadi, Richard M. Wiard, Laurent Giovangrandi, and G. T. A. Kovacs. Robust ballistocardiogram acquisition for home monitoring. *Physiological Measurement*, 30(2):169–185, jan 2009.

[124] Miguel A. García-González, A. Argelagós, Mireya Fernández-Chimeno, and Juan Ramos-Castro. Differences in qrs locations due to ecg lead: Relationship with breathing. In Laura M. Roa Romero, editor, *XIII Mediterranean Conference on Medical and Biological Engineering and Computing 2013*, pages 962–964, Cham, 2014. Springer International Publishing.

[125] Miguel A. Garcia-Gonzalez, Ariadna Argelagos-Palau, Mireya Fernandez-Chimeno, and Juan Ramos-Castro. A comparison of heartbeat detectors for the seismocardiogram. In *Computing in Cardiology*, 2013.

[126] Ary L. Goldberger, Luis A. N. Amaral, Leon Glass, Jeffrey M. Hausdorff, Plamen C. Ivanov, Roger G. Mark, Joseph E. Mietus, George B. Moody, Chung-Kang Peng, and H. Eugene Stanley. PhysioBank, PhysioToolkit, and PhysioNet. *Circulation*, 101(23), jun 2000.

[127] Tilendra Choudhary, L. N. Sharma, and Manas K. Bhuyan. Automatic Detection of Aortic Valve Opening Using Seismocardiography in Healthy Individuals. *IEEE Journal of Biomedical and Health Informatics*, 23(3):1032–1040, may 2019.

[128] Loc Luu and Anh Dinh. Using Moving Average Method to Recognize Systole and Diastole on Seismocardiogram without ECG Signal. In *2018 40th Annual*

International Conference of the IEEE Engineering in Medicine and Biology Society (EMBC), pages 3796–3799. IEEE, jul 2018.

[129] Alexandre Laurin, Farzad Khosrow-Khavar, Andrew P. Blaber, and Kouhyar Tavakolian. Accurate and consistent automatic seismocardiogram annotation without concurrent ECG. *Physiological Measurement*, 37(9):1588–1604, sep 2016.

[130] Farzad Khosrow-khavar, Kouhyar Tavakolian, and Carlo Menon. Moving toward automatic and standalone delineation of seismocardiogram signal. In *2015 37th Annual International Conference of the IEEE Engineering in Medicine and Biology Society (EMBC)*, pages 7163–7166. IEEE, aug 2015.

[131] Matti Kaisti, Mojtaba J. Tadi, Olli Lahdenoja, Tero Hurnanen, Antti Saraste, Mikko Pankaala, and Tero Koivisto. Stand-Alone Heartbeat Detection in Multidimensional Mechanocardiograms. *IEEE Sensors Journal*, 19(1):234–242, jan 2019.

[132] Federica Landreani, Damien Golier, Amin Hossein, Jérémy Rabineau, Philippe Van de Borne, Enrico Caiani, and Pierre-François Migeotte. Heartbeat Detection Using Three-Axial Seismocardiogram Acquired by Mobile Phone. In *2018 Computing in Cardiology Conference (CinC)*, volume 45, pages 1–4, dec 2018.

[133] Hiren K. Thakkar and Prasan K. Sahoo. Towards Automatic and Fast Annotation of Seismocardiogram Signals Using Machine Learning. *IEEE Sensors Journal*, 20(5):2578–2589, mar 2020.

[134] Ziran He, Min Wang, Qingsong Xie, Guoxing Wang, Yang Zhao, Yong Lian, Bo Meng, and Zhengchun Peng. A Heart Rate Measurement System Based on Ballistocardiogram for Smart Furniture. In *2018 IEEE Asia Pacific Conference on Circuits and Systems (APCCAS)*, pages 151–154. IEEE, oct 2018.

[135] Carlos Alvarado-Serrano, Pablo S. Luna-Lozano, and Ramon Pallàs-Areny. An algorithm for beat-to-beat heart rate detection from the BCG based on

the continuous spline wavelet transform. *Biomedical Signal Processing and Control*, 27:96–102, may 2016.

[136] Yu Yao, Christoph Bruser, Uwe Pietrzyk, Steffen Leonhardt, Stefan van Waasen, and Michael Schiek. Model-Based Verification of a Non-Linear Separation Scheme for Ballistocardiography. *IEEE Journal of Biomedical and Health Informatics*, 18(1):174–182, jan 2014.

[137] Ahmad Suliman, Charles Carlson, Steve Warren, and David Thompson. Performance Evaluation of Processing Methods for Ballistocardiogram Peak Detection. In *2018 40th Annual International Conference of the IEEE Engineering in Medicine and Biology Society (EMBC)*, pages 502–505. IEEE, jul 2018.

[138] Rui Ma, Qi Hao, Xiaoli Hu, and Cong Wang. Space Coding Schemes for Multiple Human Localization With Fiber-Optic Sensors. *IEEE Sensors Journal*, 18(11):4643–4653, jun 2018.

[139] Ibrahim Al-Naimi and Chi B. Wong. Indoor human detection and tracking using advanced smart floor. In *2017 8th International Conference on Information and Communication Systems (ICICS)*, pages 34–39. IEEE, apr 2017.

Notes

The same author has already published part of the work presented in this document in the following papers:

- N. Mora, F. Cocconcelli, G. Matrella and P. Ciampolini, "Fully Automated Annotation of Seismocardiogram for Noninvasive Vital Sign Measurements," in IEEE Transactions on Instrumentation and Measurement, vol. 69, no. 4, pp. 1241-1250, April 2020, doi: 10.1109/TIM.2019.2908511.

- Mora, N.; Cocconcelli, F.; Matrella, G.; Ciampolini, P. Detection and Analysis of Heartbeats in Seismocardiogram Signals. Sensors 2020, 20, 1670. https://doi.org/10.3390/s20061670

- N. Mora, F. Cocconcelli, G. Matrella and P. Ciampolini, "Accurate Heartbeat Detection on Ballistocardiogram Accelerometric Traces," in IEEE Transactions on Instrumentation and Measurement, vol. 69, no. 11, pp. 9000-9009, Nov. 2020, doi: 10.1109/TIM.2020.2998644.

- F. Cocconcelli, N. Mora, G. Matrella and P. Ciampolini, "Seismocardiography-based detection of heartbeats for continuous monitoring of vital signs," 2019 11th Computer Science and Electronic Engineering (CEEC), 2019, pp. 53-58, doi: 10.1109/CEEC47804.2019.8974343.

- Mora, N.; Cocconcelli, F.; Matrella, G.; Ciampolini, P. A Unified Methodology for Heartbeats Detection in Seismocardiogram and Ballistocardiogram Signals. Computers 2020, 9, 41. https://doi.org/10.3390/computers9020041

- F. Cocconcelli, N. Mora, G. Matrella and P. Ciampolini, "High-Accuracy, Unsupervised Annotation of Seismocardiogram Traces for Heart Rate Monitoring," in IEEE Transactions on Instrumentation and Measurement, vol. 69, no. 9, pp. 6372-6380, Sept. 2020, doi: 10.1109/TIM.2020.2967135.

- N. Mora, F. Cocconcelli, G. Matrella, G. Chiorboli and P. Ciampolini, "An accurate and stable bed-based ballistocardiogram measurement and analysis system," 2021 IEEE International Workshop on Metrology for Industry 4.0 & IoT (MetroInd4.0&IoT), 2021, pp. 482-487, doi: 10.1109/MetroInd4.0IoT51437.2021.9488475.

Acknowledgements/Ringraziamenti

The purpose of an acknowledgements section should be to express gratitude and appreciation to those who have contributed to reaching an achievement or completing something important. Thus, I think that such appreciation should be understood by those to which it is expressed. For this reason, and because the people I want to thank are (partially) non-English speakers, the following paragraph is written in Italian.

Non sono un grande amante degli elogi e dei ringraziamenti, mi mettono in imbarazzo. È però necessario che io dia credito a chi, in un modo o nell'altro, mi ha aiutato durante questi tre anni di lavoro. Cercherò però di seguire la mia indole tenendo questa sezione il più breve possibile; non sentitevi quindi offesi se non siete citati per nome.

Al Professore Paolo Ciampolini, al Professore Guido Matrella e al Professore Niccolò Mora un grazie sentito per avermi accompagnato, istruito, e consigliato durante questi anni.
Irrinunciabili i ringraziamenti a David e a Ion, i quali mi hanno aiutato a portare a compimento un grande progetto.
Un grazie alla mia famiglia, la quale mi supporta, sopporta, ascolta e ogni giorno fa mille altre cose per me.
Grazie agli amici di una vita e a quelli trovati lungo la strada, i quali mi rendono spensierato quando i pensieri sono tanti e mi strappano un sorriso ogni volta che serve.